J. Fluid Mech. (2013), *vol.* 733, *pp.* 558–587.
doi:10.1017/jfm.2013.451

Numerical study of the effect of surface waves on turbulence underneath. Part 1. Mean flow and turbulence vorticity

Xin Guo and Lian Shen†

Department of Mechanical Engineering and St. Anthony Falls Laboratory, University of Minnesota, Minneapolis, MN 55455, USA

(Received 1 August 2011; revised 21 May 2013; accepted 24 August 2013; first published online 25 September 2013)

Direct numerical simulation is performed to study the effect of progressive gravity waves on turbulence underneath. The Navier–Stokes equations subject to fully nonlinear kinematic and dynamic free-surface boundary conditions are simulated on a surface-following mapped grid using a fractional-step scheme with a pseudo-spectral method in the horizontal directions and a finite-difference method in the vertical direction. To facilitate a mechanistic study that focuses on the fundamental physics of wave–turbulence interaction, the wave and turbulence fields are set up precisely in the simulation: a pressure-forcing method is used to generate and maintain the progressive wave being investigated and to suppress other wave components, and a random forcing method is used to produce statistically steady, homogeneous turbulence in the bulk flow beneath the surface wave. Cases with various moderate-to-large turbulence-to-wave time ratios and wave steepnesses are considered. Study of the turbulence velocity spectrum shows that the turbulence is dynamically forced by the surface wave. Mean flow and turbulence vorticity are studied in both the Eulerian and Lagrangian frames of the wave. In the Eulerian frame, statistics of the underlying turbulence field indicates that the magnitude of turbulence vorticity and the inclination angle of vortices are dependent on the wave phase. In the Lagrangian frame, wave properties and the accumulative effect on turbulence vorticity are studied. It is shown that vertical vortices are tilted in the wave propagation direction due to the cumulative effects of both the Stokes drift velocity and the correlation between turbulence fluctuations and wave strain rate, whereas for streamwise vortices, these two factors offset each other and result in a negligible tilting effect.

Key words: turbulent flows, wave–turbulence interactions, waves/free-surface flows

1. Introduction

The interaction of hydrodynamic turbulence with surface waves is important to many applications. For example, the turbulence mixing and transport in the upper ocean, directly influenced by surface waves, is essential to the study of atmosphere–ocean interaction, which affects weather and climate change, marine ecosystems, and the transport of pollutants such as oil slicks. For the modelling of wavefield evolution,

† Email address for correspondence: shen@umn.edu

the energy flux from non-breaking waves to turbulence is another possibly important mechanism for wave dissipation besides wave breaking (see e.g. Cavaleri *et al.* 2007).

This study seeks to use direct numerical simulation (DNS) to obtain an improved understanding of the fundamental mechanism of the effect of waves on turbulence underneath. A wave affects the subsurface turbulence via the free-surface kinematic and dynamic boundary conditions, which require the wave surface to be material and the stress to be balanced across the surface. The orbital velocity of the wave generates a periodically alternating strain field that distorts the turbulence. Moreover, the wave's nonlinearity produces mass transport (Stokes drift) in the wave propagation direction, which leads to a mean shear from the viewpoint of the Lagrangian average. The strain rate associated with the Stokes drift velocity is typically one order of magnitude smaller than the instantaneous strain rate associated with the wave's orbital velocity, but the cumulative effect of the former can be significant. Previous studies of the above aspects of wave–turbulence interaction are briefly reviewed as follows.

The effects of the free-surface kinematic boundary condition (KBC) and the dynamic boundary condition (DBC) have long been at the heart of free-surface turbulence research. Following the rapid distortion theory (RDT) analysis by Hunt & Graham (1978), Hunt (1984) showed that the KBC and DBC respectively produce an outer (source) layer and an inner (viscous) layer at the free surface. Over the outer layer towards the free surface, vertical fluid motions are constrained (Brumley & Jirka 1987; Komori *et al.* 1993; Borue, Orszag & Staroselsky 1995; Nagaosa 1999; Shen *et al.* 1999; Variano & Cowen 2008; Campagne *et al.* 2009). Splat and antisplat events are found to be the characteristic structures of free-surface turbulence (Perot & Moin 1995; Kumar, Gupta & Banerjee 1998), and they play an important role in the turbulence kinetic energy budget near the free surface (see e.g. Guo & Shen 2010). Over the inner layer, vorticity is anisotropic and shear stress decreases drastically towards the free surface, leading to a reduction of energy dissipation near the free surface (Handler *et al.* 1993; Walker, Leighton & Garza-Rios 1996; Teixeira & Belcher 2000).

The presence of waves introduces substantial complexities to the subsurface turbulence field. In the past few decades, there have been considerable theoretical, experimental, and numerical studies of the modulation of turbulence by waves. Phillips (1961) conducted a theoretical analysis of the interaction between gravity waves and turbulence. He showed that both wave and turbulence are important to the stretching of turbulence vorticity, and there exists energy transfer from wave to turbulence via wave-strained turbulence vorticity. Craik & Leibovich (1976) and Leibovich (1980) modelled the wave effect on wind-driven surface currents using a vortex force associated with Stokes drift and local vorticity in a Craik–Leibovich (CL) equation, which is derived from the Navier–Stokes equations after Lagrangian averaging over many wave periods. They performed stability analysis and showed that the vortex force tilts vertical vortices in the wave propagation direction (Craik 1977; Leibovich 1977). For the case when the wave time scale is much smaller than the turbulence time scale, Lumley & Terray (1983) proposed a kinematic model in which frozen, isotropic turbulence is bodily convected by the orbital motion of a surface wave, and found that the turbulence energy is enhanced at harmonics of the dominant wave frequency. Thais & Magnaudet (1996) showed that when the dynamics of turbulence is dominated by wave forcing, the surface wave imposes a fixed time scale on the turbulence over a certain range of spatial scales, leading to a σ^{-3} decay rate of the temporal turbulence spectrum (see their (4.3) and figure 6). Teixeira & Belcher (2002, 2010) established a theoretical foundation by using RDT. They showed that under the periodic distortion of a surface wave, the turbulence is dependent on the wave phase. They also found that after sufficient wave periods, the Stokes drift is more effective at tilting the vertical vortices than the wind-driven shear flow. The tilting of the vertical vortices results in energy transfer from wave to turbulence.

Turbulence under waves has been measured in field and laboratory experiments (see e.g. Jiang & Street 1991; Veron, Melville & Lenain 2009). It has been found that turbulence is enhanced by surface waves (Rashidi, Hetsroni & Banerjee 1992; Thais & Magnaudet 1996). Spectral analysis showed that among turbulence eddies with different sizes, those having a characteristic time scale close to that of the wave strain rate are affected more (Kitaigorodskii *et al.* 1983; Jiang, Street & Klotz 1990; Magnaudet & Thais 1995). Direct interaction between wave and turbulence is evidenced by the strong downward bursting shown in the time series record of turbulence velocity and scalar fluctuations (Yoshikawa *et al.* 1988; Thais & Magnaudet 1996). Meanwhile, turbulence intensity has been shown to be dependent on the wave phase, and the turbulence velocity correlation that leads to Reynolds shear stress is found to be enhanced by waves (Jiang & Street 1991; Rashidi *et al.* 1992).

In numerical studies of the effect of waves on turbulence, due to the challenges in free-surface flow simulation, most of the previous work is limited to statistical descriptions that use averaging over all wave phases (see e.g. McWilliams, Sullivan & Moeng 1997; Li, Garrett & Skyllingstad 2005; Grant & Belcher 2009; Tejada-Martínez *et al.* 2009). With the increase in computing power, the much desired wave-phase-resolved simulation has become possible. Pioneering simulations of turbulence under waves have been performed by Hodges & Street (1999), Zhou (1999), Kawamura (2000), Fulgosi *et al.* (2003), and Komori *et al.* (2010). These simulations have provided substantial details on the instantaneous, three-dimensional turbulence velocity and vorticity fields, which are valuable for an improved understanding of the effect of waves on turbulence and may serve as a physical basis for future model development for this type of flow.

The present study aims at obtaining an improved understanding of the fundamental dynamics of the wave effect on subsurface turbulence via DNS of precisely set-up, well-controlled wave and turbulence fields. The canonical problem simulated is sketched in figure 1. Isotropic turbulence is generated at the centre of the computational domain. The turbulence is transported to the near-surface region and interacts with a surface wave. Both the turbulence and the wave are accurately set up. An efficacious linear random forcing method (Lundgren 2003; Rosales & Meneveau 2005; Guo & Shen 2009) is used to generate isotropic turbulence in the bulk flow under the inhomogeneous wave field. The surface wave is set up and maintained precisely with a surface pressure method, which also effectively suppresses spurious standing waves, which has been a challenging issue in free-surface flow simulation (for details see Guo & Shen 2009). Our DNS uses an accurate numerical method for undulatory surfaces developed by Yang & Shen (2011). A relatively simpler variation of the present problem, in which the dominant progressive wave is absent, was studied by Guo & Shen (2010) with a focus on small-scale, slight surface deformations and their effect on near-surface turbulence. In the present study, we investigate the effect of a long, rapid progressive wave on the underlying turbulence.

We note that our numerical set-up was inspired by the theoretical study of Teixeira & Belcher (2002), and our work is a computational counterpart of their RDT analysis for many aspects of the problem. As shown in the present paper and a companion paper, Guo & Shen (2013) (hereafter referred to as Part 2), our simulation provides rich information on the flow field to support previous theoretical predictions,

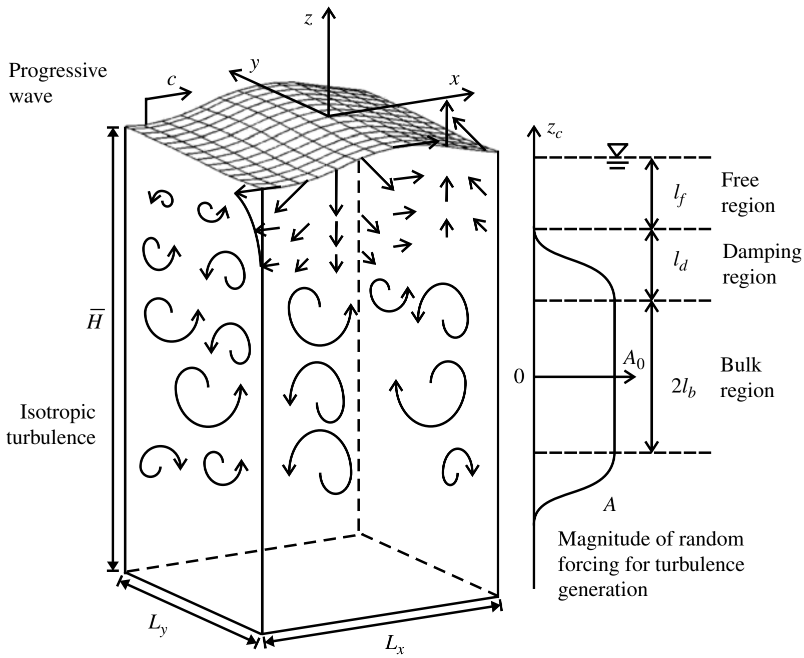

FIGURE 1. Schematics of isotropic turbulence generated in the bulk flow interacting with a progressive wave.

parametrizations, and experimental measurements. Moreover, through comprehensive analyses of the flow field in Eulerian and Lagrangian frames, our study reveals a number of examples of interesting flow physics. For example, for vortex dynamics, besides confirming the stretching effect of wave strain rate on vorticity, our result also indicates that turbulence stretching is important to the vortex evolution near the wave surface. Interestingly, vertical vortices are tilted in the streamwise direction as a cumulative effect not just by the wave's Stokes drift, as pointed out before, but also by the correlation between the wave strain rate and the turbulence vorticity; but for streamwise vortices, these two factors offset each other to produce a negligible tilting effect. For turbulence velocity fluctuations, we confirm the wave straining effect predicted by Teixeira & Belcher (2002). In addition, we discover the important role played by turbulence pressure–strain correlation and turbulence pressure transport, which counter and exceed the wave straining effect for the streamwise velocity component. For the net kinetic energy flux from wave to turbulence, we quantify the contribution of the Lagrangian effect of the wave, which compares well with previous parametrizations when the viscous effect at the surface is small. Moreover, we find that the correlation between wave and turbulence makes an appreciable contribution to the energy transfer near the wave surface, and we develop a model for this effect.

This paper is organized as follows. In § 2, we introduce our DNS approach including the problem definition, numerical scheme, and simulation parameters. In § 3, we study the mean flow and the temporal spectrum of turbulence. In § 4, we discuss the dynamics of turbulence vorticity in the Eulerian frame of the wave. In § 5, we study the Lagrangian effect of the wave on turbulence vorticity. Finally, in § 6, we present the conclusions. In Part 2 (i.e. the companion paper), we discuss the effect of the wave on Reynolds shear stress, turbulence velocity variances, and wave–turbulence energy transfer and modelling.

2. Numerical simulation

2.1. *Problem definition and numerical scheme*

As shown in figure 1, we consider DNS of a statistically steady, homogeneous turbulent flow under a progressive wave that has dynamically maintained amplitude, which is essentially unchanged as time evolves. In the simulation, the turbulence is generated by a linear random forcing method (Lundgren 2003; Rosales & Meneveau 2005), wherein a body force $\boldsymbol{f} = A\boldsymbol{u}'$ is added to the momentum equations in the physical space. Here, A is a body force parameter and $\boldsymbol{u}'$ is instantaneous turbulence velocity fluctuation. To avoid the generation of spurious interfacial phenomena, A is damped as the free surface is approached (see figure 1) according to (Guo & Shen 2009, 2010)

$$A = \begin{cases} A_0 & z_c \leqslant l_b \quad \text{bulk region,} \\ \dfrac{A_0}{2}\left[1 - \cos\left(\dfrac{\pi}{l_d}(z_c - l_b - l_d)\right)\right] & l_b < z_c \leqslant l_b + l_d \quad \text{damping region,} \\ 0 & l_b + l_d < z_c \leqslant l_b + l_d + l_f \quad \text{free region.} \end{cases} \tag{2.1}$$

Here, A_0 is the body force parameter in the bulk region; z_c is the vertical distance to the centre of the computational domain; l_b is half of the vertical length of the bulk region; l_d is the vertical length of the damping region; and l_f is the vertical length of the free region (figure 1). The progressive wave is generated and dynamically maintained in the simulation, with less than 0.1 % of variation in its amplitude, by a gentle pressure applied at the free surface. The variation of the pressure is specified using the solution of the Cauchy–Poisson problem. The details of the precise set-up of the wave and turbulence fields are documented in Guo & Shen (2009) and will not be repeated here.

The flow is in the frame (x, y, z), where x, y, and z (also denoted as x_1, x_2, and x_3) point to the streamwise (i.e. wave propagation), spanwise, and vertical directions, respectively (figure 1). The origin of the coordinate system is located at the undisturbed free surface.

The flow motions are described by the incompressible conservative-form Navier–Stokes equations

$$\frac{\partial u_i}{\partial t} + \frac{\partial (u_i u_j)}{\partial x_j} = -\frac{1}{\rho}\frac{\partial p}{\partial x_i} + \nu \frac{\partial^2 u_i}{\partial x_j \partial x_j} + A u_i', \quad i = 1, 2, 3, \tag{2.2}$$

and the continuity equation

$$\frac{\partial u_i}{\partial x_i} = 0. \tag{2.3}$$

Here, ρ is the fluid density, p is the dynamic pressure, and ν is the fluid kinematic viscosity. Note that (2.2) is written in a conservative form, which in general has better numerical performance in terms of conservation properties and accuracy in turbulence simulations compared with the non-conservative form (see e.g. Morinishi *et al.* 1998).

At the free surface, the KBC is

$$\frac{\partial \eta}{\partial t} + u\frac{\partial \eta}{\partial x} + v\frac{\partial \eta}{\partial y} - w = 0 \quad \text{at } z = \eta, \tag{2.4}$$

where η is the free-surface elevation. Neglecting the surface tension and air motion, we obtain the DBCs from the balance of stresses at $z = \eta$ as

$$\boldsymbol{t}_1 \cdot \boldsymbol{\tau} \cdot \boldsymbol{n}^{\mathrm{T}} = 0, \tag{2.5a}$$

$$\boldsymbol{t}_2 \cdot \boldsymbol{\tau} \cdot \boldsymbol{n}^{\mathrm{T}} = 0, \tag{2.5b}$$

$$\boldsymbol{n} \cdot \boldsymbol{\tau} \cdot \boldsymbol{n}^{\mathrm{T}} = -p_a. \tag{2.5c}$$

In the above equations, $\tau_{ij} = -(p - zg)\delta_{ij} + \nu(u_{i,j} + u_{j,i})$, where g is the gravitational acceleration and δ_{ij} is the Kronecker delta, p_a is the pressure on the air side, and the unit directional vectors $\boldsymbol{n}$, $\boldsymbol{t}_1$, and $\boldsymbol{t}_2$ are expressed as

$$\boldsymbol{n} = \frac{(-\eta_x, -\eta_y, 1)}{\sqrt{\eta_x^2 + \eta_y^2 + 1}}, \quad \boldsymbol{t}_1 = \frac{(1, 0, \eta_x)}{\sqrt{\eta_x^2 + 1}}, \quad \boldsymbol{t}_2 = \frac{(0, 1, \eta_y)}{\sqrt{\eta_y^2 + 1}}. \tag{2.6}$$

In (2.5), $\boldsymbol{n}^{\mathrm{T}}$ denotes the transpose of $\boldsymbol{n}$. In (2.6), η_x and η_y denote the derivatives of η with respect to x and y, respectively.

At the bottom, $z = -\overline{H}$, we apply the shear-free boundary condition. In the horizontal directions, we use periodic boundary conditions.

To ensure that the flow details near the free surface are captured adequately, we use a boundary-fitted grid system. An algebraic mapping is used to transform the irregular Cartesian space (x, y, z, t) confined by the wave surface to a rectangular computational space $(\xi, \psi, \varsigma, \iota)$ (figure 2). In the mapping, the vertical dimension is normalized by the distance from the free surface to the bottom ($\varsigma = (z + \overline{H})/(\eta + \overline{H})$), while the horizontal dimensions and the time remain the same ($\xi = x$, $\psi = y$, and $\iota = t$). Note that the grid is moving in the physical domain. The coordinate transformation for the moving grid is obtained using the chain rule for partial derivatives (Hodges & Street 1999; Yang & Shen 2011):

$$\left\{\begin{aligned} \frac{\partial}{\partial t} &= \frac{\partial}{\partial \iota} - \frac{\varsigma \eta_t}{\eta + \overline{H}}\frac{\partial}{\partial \varsigma}, \\ \frac{\partial}{\partial x} &= \frac{\partial}{\partial \xi} - \frac{\varsigma \eta_x}{\eta + \overline{H}}\frac{\partial}{\partial \varsigma}, \\ \frac{\partial}{\partial y} &= \frac{\partial}{\partial \psi} - \frac{\varsigma \eta_y}{\eta + \overline{H}}\frac{\partial}{\partial \varsigma}, \\ \frac{\partial}{\partial z} &= \frac{1}{\eta + \overline{H}}\frac{\partial}{\partial \varsigma}. \end{aligned}\right. \tag{2.7}$$

The governing equations (2.2) and (2.3) subject to the boundary conditions in terms of $(\xi, \psi, \varsigma, \iota)$ are integrated in time using a fractional-step method (Kim & Moin 1985). We remark that the numerical method used in the present paper has origins in the algebraic mapping and fractional-step method used by De Angelis, Lombardi & Banerjee (1997) and Fulgosi *et al.* (2003), who simulated a turbulent flow over a wavy boundary with sufficiently large deformation and a turbulent gas–liquid coupled flow with a freely deformed interface, respectively, and the scheme is found to be effective and accurate. The KBC is advanced in time using a second-order Runge–Kutta scheme

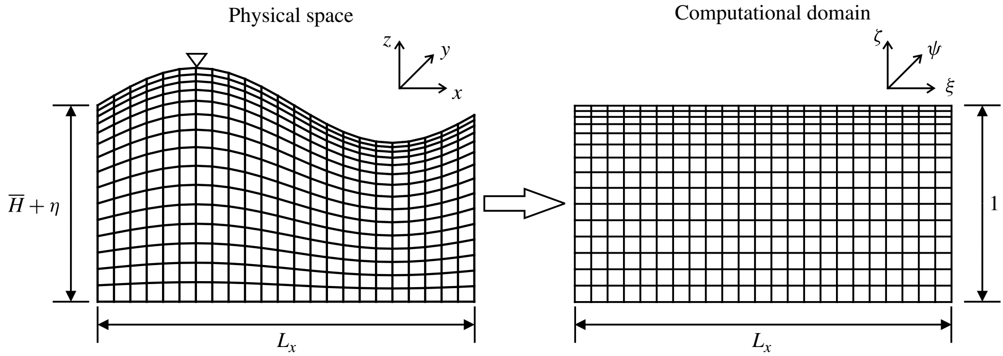

FIGURE 2. Sketch of the algebraic mapping that transforms the irregular Cartesian space (x, y, z, t) confined by the free surface into a rectangular computational domain $(\xi, \psi, \varsigma, \iota)$.

to obtain the evolution of surface elevation. For space discretization, we use a pseudo-spectral method with Fourier series in both the ξ and ψ directions; in the ς direction, we use a second-order finite-difference scheme on a staggered grid. Numerical details of our DNS and its validation are provided in Guo & Shen (2009, 2010) and Yang & Shen (2011).

2.2. *Computational parameters*

In this study, we focus on the effect of 'rapid' and 'long' waves, i.e. the time scale of the turbulence is much larger than that of the wave ($Sq/\epsilon \gg 1$) while the turbulence eddy size is much smaller than the wavelength ($L_\infty/\varLambda \ll 1$) (Kitaigorodskii & Lumley 1983), which is a common condition in upper-ocean processes (see e.g. Teixeira & Belcher 2002). Here, $S = ak\sigma$ characterizes the strength of the wave strain rate, with a being the wave amplitude, k the wavenumber, and σ the wave frequency; $q = 3(u^{rms})^2/2$ is the subsurface turbulence kinetic energy, where the superscript '*rms*' stands for root-mean-square value; ϵ is the turbulence dissipation rate; L_∞ is the turbulence integral length scale; and $\varLambda = 2\pi/k$ is the wavelength.

In our simulation, we set the dimensionless domain size as $L_x \times L_y \times L_z = 2\pi \times 2\pi \times 5\pi$. Here and hereafter, normalization is performed on the basis of a characteristic length scale L, which is $1/(2\pi)$ of the horizontal domain dimension, and a characteristic velocity scale $U = 10LA_0$ (note that $1/A_0$ is a time scale as shown in (2.1) and (2.2)). The Reynolds number is set to be $Re = UL/\nu = 1000$. In the vertical direction, $l_b = 3\pi/2$, $l_d = \pi/2$, and $l_f = \pi/2$. As shown in Guo & Shen (2009) (see their figure 7), the chosen l_b value provides a $(2\pi)^3$ cubic of isotropic turbulence in the bulk flow. Away from the bulk and towards the free surface, the forcing vanishes and the turbulence intensity reduces. The vertical variation of turbulence velocity fluctuations and length scales was studied by Guo & Shen (2009) for different l_d and l_f values. It is found that the essential physics of the turbulence generated by this linear random forcing method is insensitive to the choice of l_d and l_f. Note that $1/A_0 \sim q/\epsilon$. The value of A_0 determines the time scale and intensity of turbulence (Rosales & Meneveau 2005; Guo & Shen 2009). In this study, we fix the normalized value of A_0 to 0.1 and consider a variety of wave conditions with a focus on 'rapid' ($Sq/\epsilon \gg 1$) and 'long' ($L_\infty/\varLambda \ll 1$) waves relative to the turbulence.

The turbulence field considered here, but without the wave distortion, was studied in Guo & Shen (2010). Readers are referred there for a detailed description of the

Case	a	k	Fr	σ	S	L_∞^{cf}/Λ	Sq^{cf}/ϵ^{cf}
I_{15}	0.15	1	0.1	10	1.5	0.109	17.3
II_{10}	0.10	1	0.1	10	1	0.109	11.5
II_{15}	0.15	1	0.15	6.67	1	0.109	11.5
III_{10}	0.10	1	0.447	2.24	0.224	0.109	2.58

TABLE 1. Parameters of surface waves considered in the present study.

turbulence field. Here, we summarize the key properties. At $z^{cf} = -l_f/2$, the centre of the free region (figure 1), where the turbulence is representative of the subsurface isotropic turbulence before it interacts with the free surface, $u^{rms,cf} = 0.0897$, $\lambda^{cf} = 0.339$, and $Re_\lambda = u^{rms,cf}\lambda^{cf}/\nu = 30.4$. Here, the superscript 'cf' denotes the value at the centre of the free region, λ is the Taylor scale, and Re_λ is the Taylor-scale Reynolds number. The integral length scale is $L_\infty^{cf} = (\lambda^{cf})^2 u^{rms,cf}/(15\nu) = 0.686$, and the turbulence Reynolds number based on the integral scale is $Re_L = u^{rms,cf}(2L_\infty^{cf})/\nu = 123$. We note that the Reynolds number is relatively low due to the limitation of DNS; however, Guo & Shen (2010) showed, with extensive results, that the essential physics of free-surface turbulence is well represented by this flow. The turbulence kinetic energy is $q^{cf} = 3(u^{rms,cf})^2/2 = 0.0122$, and the turbulence dissipation rate is $\epsilon^{cf} = (u^{rms,cf})^3/L_\infty^{cf} = 0.00106$.

The parameters of the surface wave are listed in table 1. We set the dimensionless wavenumber for the prescribed wave to be $k = 1$. In other words, the dimensionless wavelength is $\Lambda = 2\pi$ and the turbulence-to-wavelength ratio is $L_\infty^{cf}/\Lambda = 0.109 \ll 1$. Because $\overline{H}/\Lambda = 5/2 > 1/2$, the surface wave considered here belongs to deep-water waves. Four cases are considered in the present study. Case II_{10} has wave amplitude $a = 0.1$, Froude number $Fr = U/\sqrt{Lg} = 0.1$, wave frequency $\sigma = (k/Fr^2)^{1/2} = 10$, wave strain rate $S = 1$, and turbulence-to-wave time ratio $Sq^{cf}/\epsilon^{cf} = 11.5 \gg 1$. To show the effect of wave nonlinearity, case II_{15} with a larger wave amplitude $a = 0.15$ and a larger Froude number $Fr = 0.15$, but the same $S = 1$ and $Sq^{cf}/\epsilon^{cf} = 11.5$, is simulated. To show the rapid distortion effect, case I_{15} with a larger $Sq^{cf}/\epsilon^{cf} = 17.3$ and case III_{10} with a smaller $Sq^{cf}/\epsilon^{cf} = 2.58$ are simulated. Compared with case II_{15}, case I_{15} has the same $a = 0.15$, a smaller $Fr = 0.1$, and a larger $S = 1.5$. Compared with case II_{10}, case III_{10} has the same $a = 0.1$, a larger $Fr = 0.447$, and a smaller $S = 0.224$. All of the cases I_{15}, II_{10}, and II_{15} belong to the rapid distortion case (see e.g. Teixeira & Belcher 2002; Chen, Meneveau & Katz 2006), and case III_{10} has a moderate distortion effect by the wave.

As shown in Guo & Shen (2010), the underlying turbulence can deform the free surface. In the absence of the prescribed dominant wave considered here, the surface deformation due to the turbulence and its effect on the underlying turbulence were studied by Guo & Shen (2010). However, for all the cases considered in our study, the Froude numbers are small. As a result, the surface deformation due to the turbulence is small compared with the amplitude of the dominant wave. For example, when $Fr = 0.447$ as in case III_{10}, which has the largest Froude number among all the cases, Guo & Shen (2010) showed that η^{rms} due to turbulence is 0.00722, which is much smaller than $a = 0.1$ or 0.15 for the prescribed dominant wave in the present paper. Therefore, here we focus on the effect of the dominant wave on the turbulence and omit the turbulence-induced surface deformation, which is of secondary importance.

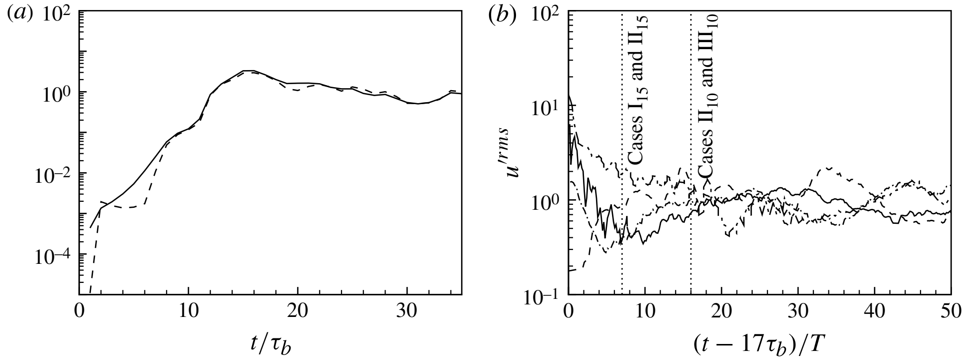

FIGURE 3. (*a*) Time history of volume-averaged turbulence kinetic energy (——) and enstrophy (– – –) in the free region and (*b*) time history of turbulence streamwise velocity variance under the wave crest for cases I_{15} (– ·· – ·· –), II_{10} (——), II_{15} (– · – · –), and III_{10} (– – –). In (*b*), the time needed for the turbulence to fully develop under the distortion of the wave as predicted by Teixeira & Belcher (2002) is marked by thin vertical dotted lines ($T_d \approx 7T$ for cases I_{15} and II_{15} and $T_d \approx 16T$ for cases II_{10} and III_{10}). In (*a*) and (*b*), the results are normalized by their time-averaged values at the steady state.

In the simulations, we use an evenly distributed grid with 128 points in the streamwise and spanwise directions. The grid size is $\Delta_x = \Delta_y = 0.0491$. In the vertical direction, we use a 348-point grid that is clustered towards the free surface. The maximum grid size is $\Delta_{z,max} = \Delta_x = 0.0491$ below the free region, and the minimum grid size is $\Delta_{z,min} = 0.00246$ at the free surface. Based on the theory of homogeneous turbulence (e.g. Tennekes & Lumley 1972), the Kolmogorov scale at the centre of the free region is estimated as $\eta_K \sim \lambda^{cf}/(15^{1/4} Re_\lambda^{1/2}) \approx 0.0313$. Therefore, we have the ratio of grid size to η_K being $1.57 < 2.1$ (note that near the surface, Δ_z is much smaller), satisfying the criterion of resolving the smallest, dissipative turbulence motion (see Pope 2000, (9.6); and Moin & Mahesh 1998). Guo & Shen (2010) showed that grid independence has been achieved for this DNS resolution for the same turbulence field without a prescribed surface wave (see their figure 3).

For the accurate simulation of the viscous effect near the free surface, boundary layers associated with the turbulence and the wave need to be resolved. For free-surface turbulence, the thickness of the viscous (inner) layer is estimated as $\delta_\nu = L_\infty^{cf}/Re_L^{1/2} = 0.0619$ (Brumley & Jirka 1987). For surface waves, the thickness of the Stokes layer is estimated as $\delta_{Stokes} = (2\nu/\sigma)^{1/2}$ (Longuet-Higgins 1953). In our simulations, the dimensionless value of δ_{Stokes} is $k\delta_{Stokes} = 0.0141$ for cases I_{15} and II_{10}, 0.0173 for case II_{15}, and 0.0299 for case III_{10}. As pointed out by Hodges & Street (1999), 5 grid points are usually necessary to capture sufficiently the viscous effect of the free surface. In the current study, we have 7, 8, and 11 points inside the Stokes layer for cases I_{15} and II_{10}, case II_{15}, and case III_{10}, respectively, and 15 points inside the viscous layer of the turbulence. As shown in the following sections, the viscous effect of the free surface is adequately resolved in our simulation.

In the present study, we conduct turbulence simulation in three steps. First, we run the simulation without the wave for a sufficiently long time to ensure that the isotropic turbulence in the bulk region is fully developed and independent of the initial condition (Rosales & Meneveau 2005). The time history of the volume-averaged turbulence kinetic energy and enstrophy in the free region is plotted in figure 3(*a*). As shown, the turbulence reached a statistically steady state at $t \approx 17\tau_b$, where τ_b is the large-eddy turnover time based on the turbulence quantities at the centre of the bulk flow. Rosales & Meneveau (2005) found that the turbulence development time depends on the spectrum of the initial turbulence field. The higher the wavenumber at which the maximum energy occurs, the longer the developing time of the turbulence. For the present problem in which the maximum energy occurs at $k = 1$, $t \approx 17\tau_b$ appears to be the time needed. Next, we apply surface pressure to generate and maintain the progressive wave until the turbulence is fully developed under the distortion of the surface wave. Teixeira & Belcher (2002) showed that the development time for turbulence under the distortion of surface wave scales as $T_d \sim 1/(a^2k^2\sigma) = T/(2\pi a^2k^2)$ (see their (3.19)). Here, $T = 2\pi/\sigma$ is the wave period. In this study, $T_d \approx 7T$ for cases I_{15} and II_{15}, and $T_d \approx 16T$ for cases II_{10} and III_{10}. The time history of the turbulence streamwise velocity variance under the wave crest is shown in figure 3(*b*). The definition of turbulence velocity fluctuation is given in appendix A. Note that only the results in the first 50 wave periods are shown in the figure for the purpose of illustration. As shown, the turbulence reaches a steady state around the time predicted by Teixeira & Belcher (2002), which is marked by the vertical lines in figure 3(*b*). Finally, after reaching the statistically steady state, the simulation is further run for $60\tau_b$ to generate sufficient data for time averaging for statistical analysis.

3. Wave field and turbulence spectrum

In this section, to understand the periodic distortion effect of the wave on the underlying turbulence, we first briefly discuss the velocity and strain rate of the wave field in § 3.1. Then, in § 3.2, we investigate the turbulence frequency spectrum to obtain a global view of the response of the turbulence to the surface wave distortion. This study focuses on case II_{10}. The other three cases are used to show comparison. Specifically, case II_{15} has the same wave distortion as case II_{10} but a stronger nonlinear effect; case I_{15} has the same nonlinear effect as case II_{15} but a stronger wave distortion; and case III_{10} has only moderate wave distortion. Hereafter, some of the figures show all of the cases if their difference or similarity is noteworthy; for the sake of brevity, some figures show only case II_{10} if the results of the other cases can be easily deduced or if words are sufficient for describing new features.

3.1. *Wave velocity and strain rate*

We show the contours of $\langle u \rangle$ and $\langle w \rangle$ in figures 4(*a*) and 4(*b*), respectively. Here and hereafter, $\langle \cdot \rangle$ denotes the wave phase average defined in appendix A. In figure 4(*a*), the wave velocity vector field $(\langle u \rangle, \langle w \rangle)$ is also plotted. For the wave orbital velocity, fluid particles move in the wave propagation direction under the wave crest and in the opposite direction under the wave trough. Under the forward and backward slopes, fluid particles rise and fall with the wave surface, respectively. As the depth increases, the magnitude of $\langle u \rangle$ and $\langle w \rangle$ decreases.

In the present study, because the wave propagates with its form essentially unchanged, it is convenient to study some of the quantities in the wave-following frame which translates horizontally with the wave phase speed c. In this frame, the mean velocity becomes $(\langle u \rangle - c, \langle w \rangle)$ as shown in figure 4(*b*). We can see that wave particles are convected to the upstream (i.e. negative direction of the 'kx–σt'-axis) along a wavy trajectory. In this study, a wave particle is defined as a fluid particle convected by the wave velocity. This moving frame is useful for some of the analyses in the following sections of this paper and in Part 2.

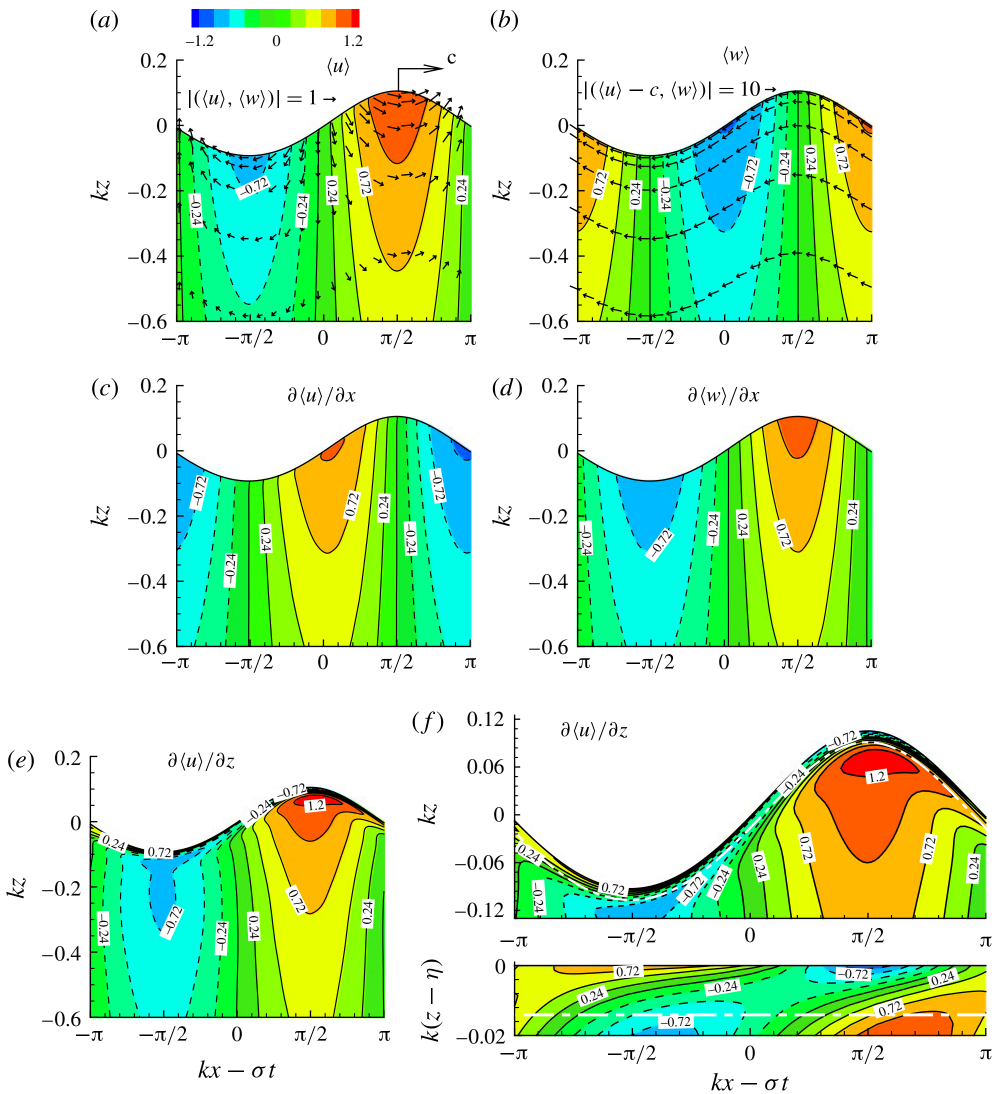

FIGURE 4. Contours of (a) $\langle u\rangle$, (b) $\langle w\rangle$, (c) $\partial\langle u\rangle/\partial x$ $(=-\partial\langle w\rangle/\partial z)$, ($d$) $\partial\langle w\rangle/\partial x$, and ($e$) $\partial\langle u\rangle/\partial z$. ($f$) Close-up view of the near-surface region in (e) with respect to the physical coordinate z (upper plot) and the distance from the free surface $z-\eta$ (lower plot). In (a) and (b), respectively, the velocity field of phase-averaged mean flow in the Earth-fixed frame $(\langle u\rangle, \langle w\rangle)$ and in the wave-following frame $(\langle u\rangle - c, \langle w\rangle)$ are also plotted. The velocity vectors are shown at every six grid points in the horizontal direction and every eight points in the vertical direction. In (f), the boundary of the Stokes layer is marked by – · – · – (white). In (a) and (b), the results are normalized by $a\sigma$. In (c) to (f), the results are normalized by S. Case II_{10} is shown here. The wave propagates from left to right.

Next, we examine velocity gradients. There are three independent wave velocity gradients, namely $\partial\langle u\rangle/\partial x$ $(=-\partial\langle w\rangle/\partial z)$, $\partial\langle w\rangle/\partial x$, and $\partial\langle u\rangle/\partial z$. Their distributions are shown in figure 4(c–f). Due to the orbital velocity of the wave (figure 4a,b), $\partial\langle u\rangle/\partial x$ is negative under the forward slope and positive under the backward slope; $\partial\langle w\rangle/\partial x$

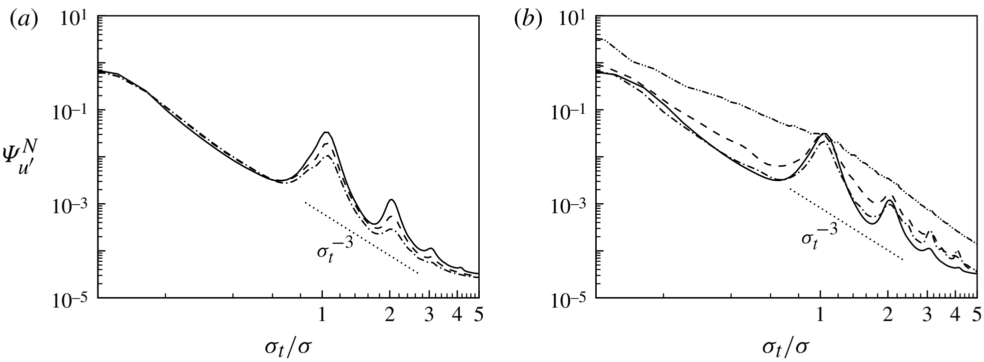

FIGURE 5. Spectrum of streamwise turbulent velocity, $\Psi_{u'}^N$: (*a*) at $kz = -0.2$ (——), $kz = -0.4$ (– – –), and $kz = -0.6$ (– · – · –) for case II_{10}; (*b*) at $kz = -0.2$ for cases I_{15} (– – –), II_{10} (——), II_{15} (– · – · –), and III_{10} (– ·· – ·· –).

is maximum under the wave crest and minimum under the wave trough. As the depth increases, the magnitude of $\partial\langle u\rangle/\partial x$ and $\partial\langle w\rangle/\partial x$ decreases.

The distribution of $\partial\langle u\rangle/\partial z$ shown in figure 4(*e*) is noteworthy. Under the wave crest, $\partial\langle u\rangle/\partial z$ is positive in the deep region. Towards the wave surface, $\partial\langle u\rangle/\partial z$ increases first and then decreases drastically to a negative value at the wave surface (see the close-up view near the wave surface shown in figure 4*f*). Under the wave trough, there is an opposite distribution of $\partial\langle u\rangle/\partial z$. That is, $\partial\langle u\rangle/\partial z$ is negative in the deep region, decreases towards the wave surface, and then increases sharply to a positive value at the wave surface. Without losing generality, we discuss $\partial\langle u\rangle/\partial z$ under the wave crest only. The positive value in the deep region and the increase of $\partial\langle u\rangle/\partial z$ towards the surface are associated with the distribution of $\langle u\rangle$ discussed earlier (figure 4*a*). At the wave surface, according to the shear-free DBC (2.5*a*), $\partial\langle u\rangle/\partial z$ and $\partial\langle w\rangle/\partial x$ at the wave surface are nearly negatively correlated (Longuet-Higgins 1992). Derivation and discussion are provided in appendix B. Near the free surface, a Stokes layer develops (see e.g. Longuet-Higgins 1953; Iskandarani & Liu 1991), within which $\partial\langle u\rangle/\partial z$ varies drastically. The boundary of the Stokes layer is marked in figure 4(*f*).

We summarize the effect of the wave strain on the deformation of fluid elements in the upper part of figure 8. Under the forward slope, fluid elements are compressed in the streamwise direction and stretched in the vertical direction. Under the backward slope, the opposite process occurs. Under the wave crest and trough, fluid elements are distorted by the 'shear' strain rate. (Note that the apparent shearing by $\partial\langle u\rangle/\partial z$ and $\partial\langle w\rangle/\partial x$ is essentially irrotational straining for the most part of the wave field.)

3.2. *Spectral characteristics of turbulence fluctuation*

Figure 5 shows the frequency spectrum of streamwise turbulent velocity defined by

$$\Psi_{u'}(\sigma_t) = \frac{1}{2\pi}\int_T \overline{u'(\boldsymbol{x},t)\,u'(\boldsymbol{x},t+\tau)}\mathrm{e}^{-\mathrm{i}\sigma_t\tau}\,\mathrm{d}\tau, \tag{3.1}$$

where '$\overline{(\cdot)}$' denotes the plane average defined in appendix A (A 5). The spectrum is normalized as

$$\Psi_{u'}^N(\sigma_t) = \frac{\Psi_{u'}(\sigma_t)}{(u'^{rms})^2}. \tag{3.2}$$

We first focus on $\Psi_{u'}^{N}(\sigma_t)$ of case II_{10} shown in figure 5(*a*). It exhibits two prominent features. First, bumps are visible at harmonics of the wave frequency σ. We have also observed similar bumps in the spectra of v' and w' (results not shown here). The origin of the bumps was discussed in detail by Lumley & Terray (1983) through the generalization of Taylor's hypothesis, where frozen, isotropic turbulence is bodily convected by the orbital motion of the surface wave. The bump at the dominant wave frequency has also been observed in previous measurements (see e.g. Kitaigorodskii *et al.* 1983; Jiang *et al.* 1990; Magnaudet & Thais 1995; Thais & Magnaudet 1996). The second feature is that there is a σ_t^{-3} decay of the spectra. Thais & Magnaudet (1996) explained this decay rate by saying that the dynamics of the turbulence is dominated by the forcing of the surface wave, and the forcing is at the fixed wave frequency for turbulence eddies of different sizes. As will be shown in the following sections and Part 2, under the wave distortion, the turbulence is dynamically forced by the surface wave, e.g. turbulence vortices are periodically stretched, compressed, and turned by the surface wave, and the wave distortion induces periodic energy exchange between the wave and turbulence.

The $\Psi_{u'}^{N}(\sigma_t)$ at different depths is also shown in figure 5(*a*). As the depth increases, the magnitude of the bumps decreases, due to the decrease of the wave strain rate. In particular at the high frequency ($\sigma_t/\sigma \geqslant 3$), the bumps almost cannot be seen at $kz < -0.4$.

In figure 5(*b*), we compare $\Psi_{u'}^{N}(\sigma_t)$ among the different cases. The bumps at harmonics of the wave frequency and the σ_t^{-3} decay of the spectra, which are observed in case II_{10}, show in all the other cases. As the wave amplitude increases (i.e. compare case II_{10} with case II_{15}), we can see that the magnitude of the bumps at high frequency is more remarkable in the latter case, due to the increase of wave nonlinearity. A comparison between cases I_{15} and II_{15} shows that for the rapid distortion case, $\Psi_{u'}^{N}(\sigma_t/\sigma)$ is insensitive to change in the wave strain rate. The $\Psi_{u'}^{N}(\sigma_t)$ of case III_{10} is noteworthy. Only one hump at the dominant wave frequency is shown, and the hump is much broader than those in the other cases, due to the much smaller turbulence-to-wave time ratio in case III_{10} (table 1), where Taylor's hypothesis may not hold.

In summary, we study in this section the velocity and strain rate of the surface wave and turbulence frequency spectrum. Under the forward and backward slopes of the surface wave, fluid particles experience the distortion of the normal strain rate; and under the wave crest and trough, fluid particles experience the distortion of the 'shear' strain rate. Our result for the turbulence frequency spectrum shows that due to the periodic forcing of the wave on turbulence, turbulence is enhanced at harmonics of the dominant wave frequency and the spectrum exhibits a σ^{-3} decay.

4. Eulerian dynamics of turbulence vorticity

In this section, we study the turbulence vorticity dynamics in the Eulerian frame of the wave to understand the effect of periodic wave distortion on the turbulence vorticity at different wave phases. In § 4.1, we examine the instantaneous turbulence field. In §§ 4.2 and 4.3, we study the statistics of vorticity intensity and vortex inclination angle to understand respectively the compressing/stretching and shear effects of the wave on the turbulence vortices below. In this study, vorticity is defined as the curl of fluid velocity, $\boldsymbol{\omega} = \nabla \times \boldsymbol{u}$. Vortices refer to vortical structures with concentration of aligned vorticity, which are educed by the iso-surface of negative λ_2 (Jeong & Hussain 1995). Here, λ_2 is the second largest eigenvalue of $\boldsymbol{S}^2 + \boldsymbol{\Omega}^2$, with $S_{ij} = (u_{i,j} + u_{j,i})/2$ and $\Omega_{ij} = (u_{i,j} - u_{j,i})/2$. As shown in Jeong & Hussain (1995) and other studies, in turbulent flows, the effect of convective terms on the local pressure is

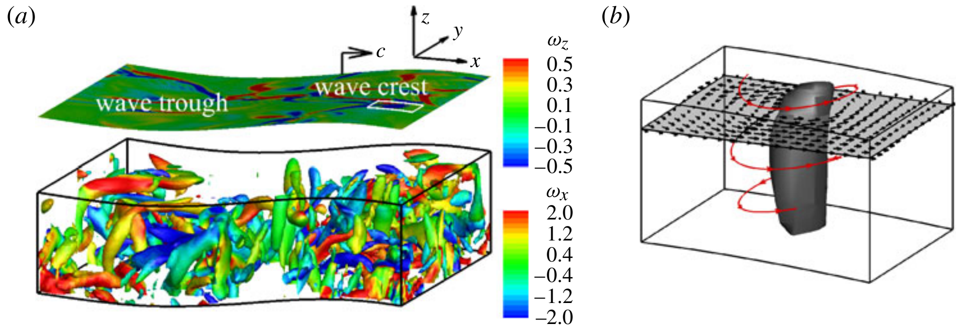

FIGURE 6. (*a*) Instantaneous turbulence vortical structures. In the flow, the iso-surface of $\lambda_2 = -0.2$ is shown with contours of ω_x. The wave surface is lifted up for better visualization. Contours of ω_z are shown on the wave surface. The arrow denotes the wave propagation direction. (*b*) Close-up view of the surface-connected vortex marked in (*a*) with a white box on the free surface. The turbulence velocity vector (u', v') is shown at $kz = -0.05$. A representative helical streamline is plotted. Case II_{10} is shown here.

larger than the unsteady effect and viscous effect. Consequently, the low pressure in a vortex core corresponds to negative values of λ_2 (see the analysis in Jeong & Hussain 1995), and the iso-surfaces of negative λ_2 can be used to educe vortical structures.

4.1. *Instantaneous turbulence vorticity field*

A representative snapshot of instantaneous turbulence vortical structures is shown in figure 6(*a*). As shown, the turbulence vortical structures are mostly in the streamwise and vertical directions. Under the wave trough, vortical structures have strong ω_x; under the wave crest, vertical vortices are more obvious. We also plot the contours of ω_z on the wave surface. It shows that there is a dependence of ω_z on the wave phase, with ω_z being stronger at the wave crest than at the wave trough. We find that the vertical vortical structures tilt in the wave propagation direction at all the wave phases. It is noted that ω_z on the wave surface corresponds to surface-connected vortices. Observation of the instantaneous flow field indicates that the surface-connected vortices exist in regions with turbulent downwelling motion, where whirlpool-like structures are formed. Lombardi, De Angelis & Banerjee (1996) simulated gas–liquid flow with a flat interface and detected whirlpool-like structures in the form of the attachment of quasi-streamwise vortices to the free surface. Pan & Banerjee (1995) observed surface-connected vortices for free-surface flow without surface shear and found that surface-connected vortices exist for a long period until they are destroyed by upwellings. They also found that the surface-connected vortices can pair and merge, and they decay slowly. A close-up view of a typical surface-connected vortex from figure 6(*a*) is shown in figure 6(*b*), where a representative streamline is also plotted. The vortex is stretched vertically, which is important to the evolution of turbulence vorticity. Similar vortex stretching by turbulence velocity fluctuations is also observed for the streamwise vortices. Our results for the conditional average on streamwise and vertical vortices (not shown here) indicate that this turbulence vortex stretching effect exists at all the wave phases and is as important as the wave straining effect.

Next, statistical evidence of the phase dependence of vorticity distribution is provided in §§ 4.2 and 4.3. The cumulative effect of waves on vortical structures is studied with the Lagrangian average in § 5.

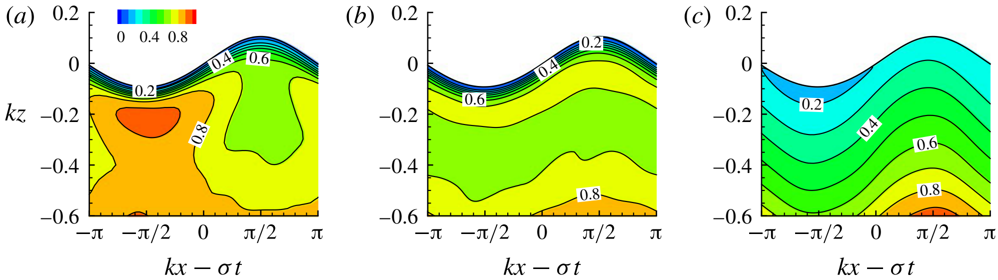

FIGURE 7. Contours of (*a*) $\langle \omega_x'^2 \rangle/(\omega_x'^{rms,cf})^2$, (*b*) $\langle \omega_y'^2 \rangle/(\omega_y'^{rms,cf})^2$, and (*c*) $\langle \omega_z'^2 \rangle/(\omega_z'^{rms,cf})^2$. The wave propagates from left to right. Case II_{10} is shown here.

4.2. *Statistics of vorticity intensity*

Figure 7 shows the distribution of phase-averaged enstrophy components $\langle \omega_i'^2 \rangle$. As shown in figure 7(*a*), high intensity of $\langle \omega_x'^2 \rangle$ is located under the wave trough, whereas low intensity is under the wave crest. Towards the wave surface, $\langle \omega_x'^2 \rangle$ decreases sharply over the region $k(z-\eta) > -0.1$. This decrease is due to the shear-free boundary condition at the wave surface (see e.g. Walker *et al.* 1996; Shen *et al.* 1999).

The distribution of $\langle \omega_y'^2 \rangle$ is shown in figure 7(*b*). The shape of the contour lines is similar to the wave surface, indicating that the dependence of $\langle \omega_y'^2 \rangle$ on the wave phase is weak. In the vertical direction, as the wave surface is approached, $\langle \omega_y'^2 \rangle$ decreases drastically within the region $k(z-\eta) > -0.1$, also due to the shear-free boundary condition.

Figure 7(*c*) plots the distribution of $\langle \omega_z'^2 \rangle$. It shows that high intensity of $\langle \omega_z'^2 \rangle$ is located under the wave crest, while low intensity is under the wave trough. Because the effect of the free surface on ω_z is relatively small (see e.g. Pan & Banerjee 1995; Walker *et al.* 1996; Shen *et al.* 1999), the variation of $\langle \omega_z'^2 \rangle$ near the surface is mainly due to the effect of the surface wave.

4.3. *Statistics of vortex inclination angle*

To further understand the distribution of turbulence vorticity under a surface wave, following Shen *et al.* (1999), we study the inclination angle of the projection of vorticity vectors onto the *x*–*z* plane:

$$\varphi_{xz} = \arctan\left(\frac{\omega_z}{\omega_x}\right). \tag{4.1}$$

The histogram of φ_{xz} at a representative depth at different wave phases is plotted in figure 8. To highlight strong vortical events, the statistics is weighted by $\omega_x^2 + \omega_z^2$ (Shen *et al.* 1999). The result is plotted in a polar coordinate system. The azimuth corresponds to φ_{xz}, and the radius represents the histogram at the angle. In figure 8, we also sketch the straining effect on fluid elements. Note that the wave propagates from left to right; relative to the wave form, vortical structures travel from right to left (see figure 4*b*) while experiencing the strain field shown in figure 8.

For case II_{10} shown in figure 8, we first discuss the values of peak φ_{xz}, i.e. the angle at which the histogram is maximum. As shown, φ_{xz} is in the neighbourhood of $0°/180°$ and $90°/270°$, corresponding to streamwise and vertical vortices, respectively.

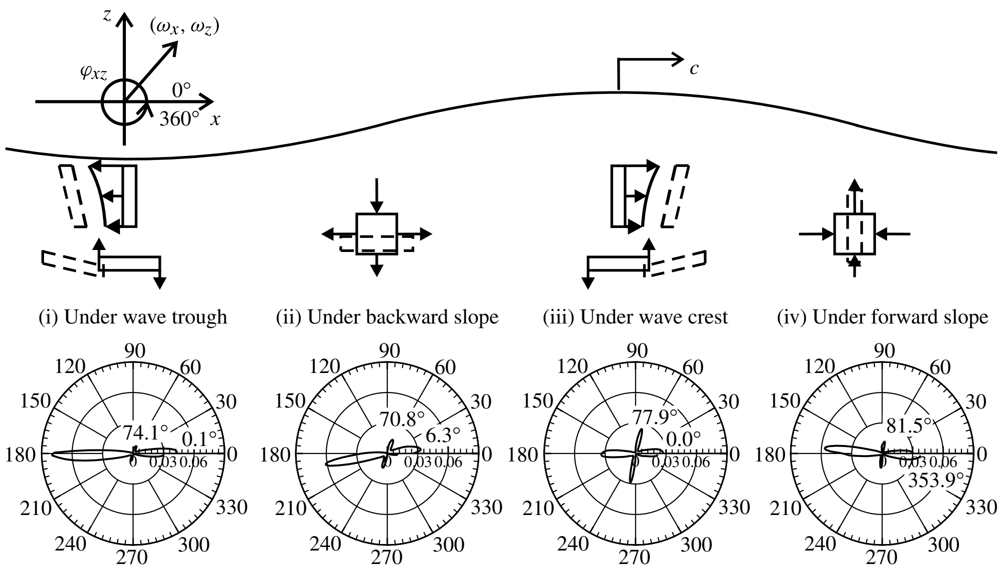

FIGURE 8. Histogram of φ_{xz} under: (i) wave trough ($kx - \sigma t = -\pi/2$); (ii) backward slope ($kx - \sigma t = 0$); (iii) wave crest ($kx - \sigma t = \pi/2$); (iv) forward slope ($kx - \sigma t = \pi$). $k(z - \eta) = -0.05$. The φ_{xz} values for the highest histograms for streamwise and vertical vortices are marked in the plots. Case II_{10} is shown here. The sign convention of φ_{xz} is sketched in the top left corner. The distortion effect of the wave strain field on fluid elements is sketched in the upper part with solid and dashed lines representing early and later times, respectively.

For streamwise vortices, under the forward slope (plot iv), the peak of distribution is located within the second and fourth quadrants (around 174°/354°); under the backward slope (plot ii), the peak is located in the first and third quadrants (around 6°/186°). In general, the inclination of streamwise vortices follows the slope of the surface elevation. The variation of peak φ_{xz} is due to the wave turning effect, which vortices experience under the wave trough and crest. That is, streamwise vortices are turned to the clockwise (resp. anticlockwise) direction under the wave trough (resp. crest), as shown in the sketch of the wave straining effect in figure 8.

For vertical vortices, the peak φ_{xz} is around 82°/262° under the forward slope (plot iv), around 78°/258° under the wave crest (plot iii), around 71°/251° under the backward slope (plot ii), and around 74°/254° under the wave trough (plot i). The variation is because vertical vortices are turned to the anticlockwise (resp. clockwise) direction under the wave trough (resp. crest) (figure 8). Despite the oscillation, the peak φ_{xz} of vertical vortices is located in the first and third quadrants at all the wave phases, indicating that the clockwise tilting of vertical vortices dominates the anticlockwise tilting (Teixeira & Belcher 2002). We also note that the backward slope (plot ii) is special: the tilting effect is maximum there, and both the streamwise and vertical vortices are located in the first and third quadrants. As will be shown in Part 2, the tilted vortices affect the Reynolds shear stress $\langle u'w' \rangle$, especially beneath the wave's backward slope.

Next, we examine the magnitude of the histogram in figure 8. Comparing the streamwise and vertical vortices, we find that under the wave crest (plot iii), the vertical vortices are comparable to the streamwise ones; under the wave trough (plot i),

Case	Under wave trough		Under backward slope		Under wave crest		Under forward slope	
	φ_{xz,ω_x}	φ_{xz,ω_z}	φ_{xz,ω_x}	φ_{xz,ω_z}	φ_{xz,ω_x}	φ_{xz,ω_z}	φ_{xz,ω_x}	φ_{xz,ω_z}
I_{15}	2.7°	70.5°	10.5°	59.5°	1.8°	75.0°	352.3°	84.2°
II_{10}	0.1°	74.1°	6.3°	70.8°	0.0°	77.9°	353.9°	81.5°
II_{15}	359.9°	73.3°	10.5°	59.8°	0.0°	75.9°	353.6°	85.7°
III_{10}	0.0°	84.7°	5.6°	82.6°	0.0°	84.0°	354.6°	88.3°

TABLE 2. The φ_{xz} values for the highest histograms for streamwise and vertical vortices.

the streamwise vortices dominate. This variation is related to the vortex stretching and compression effects of the wave strain field. Under the forward slope, the streamwise vortices are compressed and the vertical vortices are stretched, and under the backward slope, the process reverses (figure 8). Note that relative to the wave, vortices move in the opposite direction to wave propagation. The (locally) cumulative effect of wave straining makes the streamwise vorticity minimum (resp. maximum) and the vertical vorticity maximum (resp. minimum) under the wave crest (resp. trough). This vortex stretching and compression by local wave strain is consistent with the theoretical description of turbulence vorticity evolution under a surface wave (Teixeira & Belcher 2002, see their figure 6).

For cases I_{15}, II_{15}, and III_{10}, the wave strain affects the turbulence vorticity in a similar way to that in case II_{10}. The φ_{xz} values for the highest histograms for streamwise and vertical vortices are listed in table 2. A comparison of case II_{10} with the other cases shows that the tilting of vortices is more obvious in cases I_{15} and II_{15} and less obvious in case III_{10} than that in case II_{10}. For example, under the backward slope, the peak φ_{xz} for vertical vortices is 59.5°/239.5° in case I_{15}, 70.8°/250.8° in case II_{10}, 59.8°/239.8° in case II_{15}, and 82.6°/262.6° in case III_{10}. As will be shown in the following sections and Part 2, compared to case II_{10}, the cumulative effect of vortex tilting by the wave is enhanced (relative to other effects such as the stretching by turbulence) in cases I_{15} and II_{15} and reduced in case III_{10} due to the difference in the wave strain rate and wave nonlinearity and, as a result, the Reynolds shear stress is different between the different cases.

We summarize the Eulerian effect of a surface wave on turbulence vorticity in figure 9(*a*). Under the backward slope, the wave strain enhances the streamwise vorticity and weakens the vertical vorticity. Under the forward slope, the opposite process occurs. Under the wave trough, the wave turns streamwise and vertical vortices in the clockwise and anticlockwise directions, respectively; and the turning process reverses under the wave crest. Overall, there exists a cumulative effect of tilting vertical vortices in the clockwise direction. This cumulative effect is further discussed in the Lagrangian frame in § 5 below. The vortices are also strengthened due to the stretching by turbulence velocity fluctuations.

5. Lagrangian dynamics of turbulence vorticity

In this section, we discuss the cumulative effect of a surface wave on turbulence vorticity induced by the Lagrangian properties of surface waves. The Lagrangian effect of a surface wave is due to the wave's nonlinearity, and can be quantified in the Lagrangian frame by the Lagrangian average operator, '$\overline{(\cdot)}^L$', defined in appendix A, via the tracking of wave particles convected by the wave velocity. Compared with the

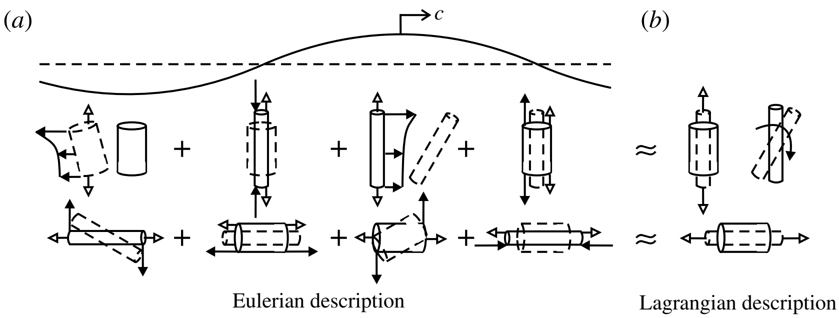

FIGURE 9. Sketch of the evolution of turbulence vortices under a progressive wave: (*a*) Eulerian description, (*b*) Lagrangian description. The effect of wave strain is denoted by solid arrows, and the effect of turbulence fluctuations is denoted by hollow arrows. Cylinders denote turbulence vortical structures. Solid and dashed lines represent early and later times, respectively. The Lagrangian effect is discussed in § 5.2.

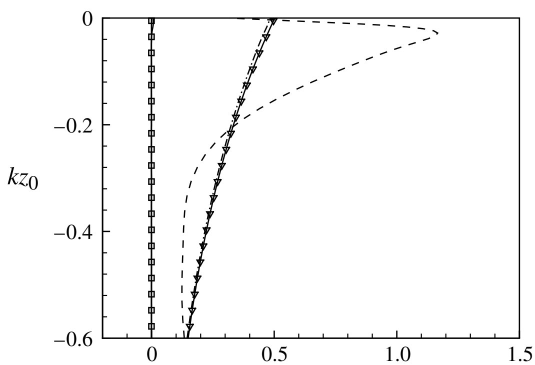

FIGURE 10. Vertical profiles of $\overline{\partial\langle u\rangle/\partial x}^L$ (——), $\overline{\partial\langle w\rangle/\partial x}^L$ (– · – · –), $\overline{\partial\langle u\rangle/\partial z}^L$ (– – –) from the present DNS, and $\overline{\partial\langle u\rangle/\partial x}^L$ (—□—) and $\overline{\partial\langle w\rangle/\partial x}^L = \overline{\partial\langle u\rangle/\partial z}^L$ (—▽—) based on fifth-order Stokes theory (Fenton 1985). Results are normalized by $2akS$. Case II_{10} is shown here.

periodic effect of the wave distortion on turbulence vorticity in the Eulerian frame discussed in § 4, the analysis in the Lagrangian frame quantifies the net effect of surface wave on turbulence vorticity after the distortion over many wave periods. In § 5.1, we first study the Lagrangian properties of surface waves. In § 5.2, we apply the Lagrangian average operator to the vortex evolution equation to investigate the wave's cumulative effect on turbulence vorticity.

5.1. *Lagrangian wave field*

We first discuss the Lagrangian properties of the surface wave. Because § 5.1 focuses on the wave field, for which the essential physics is similar among cases I_{15}, II_{10}, II_{15}, and III_{10}, we show results for case II_{10} only. The differences between these cases are manifested in the turbulence field, which is discussed in § 5.2 and Part 2.

The Lagrangian average of the wave strain rate, $\overline{\partial\langle u\rangle/\partial x}^L = -\overline{\partial\langle w\rangle/\partial z}^L$, $\overline{\partial\langle w\rangle/\partial x}^L$, and $\overline{\partial\langle u\rangle/\partial z}^L$, is plotted in figure 10. To help understand these Lagrangian quantities,

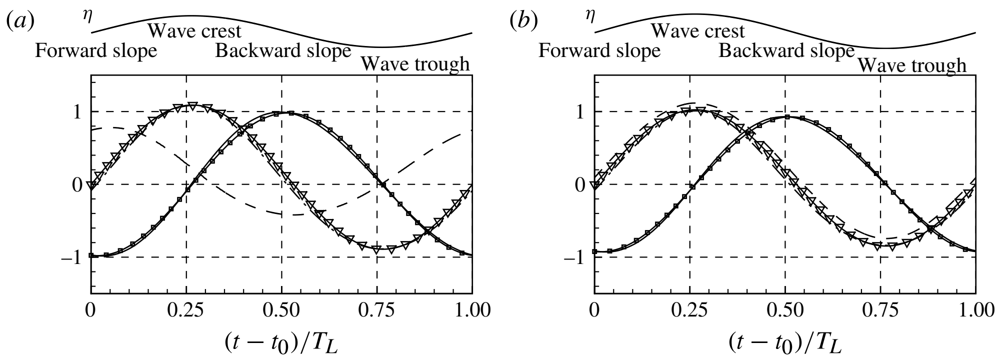

FIGURE 11. Variations of $\partial\langle u\rangle/\partial x$ $(=-\partial\langle w\rangle/\partial z)$ (——), $\partial\langle w\rangle/\partial x$ (– · – · –), $\partial\langle u\rangle/\partial z$ (– – –) from the present DNS, and $\overline{\partial\langle u\rangle/\partial x}^L$ (—□—) and $\overline{\partial\langle w\rangle/\partial x}^L = \overline{\partial\langle u\rangle/\partial z}^L$ (—▽—) based on fifth-order Stokes theory (Fenton 1985) along the trajectory of a wave particle initially located at (*a*) $(kx - \sigma t = \pi, k(z-\eta) = -k\delta_{Stokes}/2)$ and (*b*) $(kx - \sigma t = \pi, k(z-\eta) = -5k\delta_{Stokes})$ during a T_L period. The result is normalized by S. The corresponding surface elevation above the particle as it travels is sketched at the top. Case II_{10} is shown here.

we plot the variations of $\partial\langle u\rangle/\partial x$, $\partial\langle w\rangle/\partial x$, and $\partial\langle u\rangle/\partial z$ along the wave particle trajectory in figure 11. Two representative depths for the particle are chosen. In figure 11(*a*), the results for a near-surface particle initially located at $(kx - \sigma t = \pi$, $k(z-\eta) = -k\delta_{Stokes}/2)$ are plotted; figure 11(*b*) is for a particle initially located at $(kx - \sigma t = \pi,\ k(z-\eta) = -5k\delta_{Stokes})$. As a comparison, the results based on the fifth-order potential Stokes theory (Fenton 1985) are also plotted in figures 10 and 11. Note that because the theory is based on the potential flow solution, $\partial\langle u\rangle/\partial z = \partial\langle w\rangle/\partial x$. The comparison between the present DNS and Stokes theory indicates that the viscous effect is mainly on $\partial\langle u\rangle/\partial z$ rather than on $\partial\langle u\rangle/\partial x$ and $\partial\langle w\rangle/\partial x$, consistent with the results shown in figure 4. To further understand the effect of viscosity on the wave velocity field, we have also applied the Helmholtz decomposition to the wave velocity, decomposed it into an irrotational component and a rotational component, and performed the same analysis (results not shown here). We have drawn the same conclusion, i.e. the irrotational component is consistent with the potential Stokes theory, and the rotational component is noteworthy in $\partial\langle u\rangle/\partial z$ and is about zero in $\partial\langle u\rangle/\partial x$ and $\partial\langle w\rangle/\partial x$.

As shown in figure 10, $\overline{\partial\langle u\rangle/\partial x}^L$ is small, because the positive $\partial\langle u\rangle/\partial x$ under the backward slope and the negative $\partial\langle u\rangle/\partial x$ under the forward slope is nearly antisymmetric (figure 4*c*), and the time spent by a particle under the forward and backward slopes is about the same (figure 11).

For $\overline{\partial\langle w\rangle/\partial x}^L$, it is positive and increases towards the free surface. This is because the magnitude of the positive $\partial\langle w\rangle/\partial x$ under the wave crest is larger than the negative one under the wave trough due to wave nonlinearity, and fluid particles spend more time under the wave crest than under the wave trough (figure 11), consistent with previous theoretical analysis (Fenton 1985) and measurement (Elliott 1953; Morison & Crooke 1953).

The distribution of $\overline{\partial\langle u\rangle/\partial z}^L$ is noteworthy. Towards the free surface, it increases first, reaches its maximum, and then decreases drastically to a small value at the free surface. The increase is due to the larger magnitude of positive $\partial\langle u\rangle/\partial z$ under the wave crest compared with the negative one under the wave trough (figure 11*b*) and the greater time spent by fluid particles under the wave crest. The decrease is due to the viscous effect of the free surface discussed in § 3. From (B 2), we have

$$\overline{\frac{\partial\langle u\rangle}{\partial z}}^L = -\overline{\frac{\partial\langle w\rangle}{\partial x}}^L - \overline{\frac{4\eta_x}{1-\eta_x^2}\frac{\partial\langle w\rangle}{\partial z}}^L \tag{5.1}$$

at the wave surface. Due to the negative correlation between η_x (of $O(ak)$) and $\partial\langle w\rangle/\partial z$ (of $O(S)$) at the wave surface (§ 3.1), we estimate the second term on the right-hand side of (5.1) as

$$-\overline{\frac{4\eta_x}{1-\eta_x^2}\frac{\partial\langle w\rangle}{\partial z}}^L \sim O(2akS). \tag{5.2}$$

The $\overline{\partial\langle w\rangle/\partial x}^L$ (the first term in (5.1)) is also comparable to akS (see figure 10). As a result, the summation of the two terms on the right-hand side of (5.1) leads to $\overline{\partial\langle u\rangle/\partial z}^L$ of $O(akS)$ at the wave surface. The viscous effect is mainly in the Stokes layer (§ 3.1).

To further understand the viscous effect on $\overline{\partial\langle u\rangle/\partial z}^L$, we study the variation of $\partial\langle u\rangle/\partial z$ near the wave surface in figure 11(*a*). Compared with that in the relatively deep region (figure 11*b*), the positive (resp. negative) $\partial\langle u\rangle/\partial z$ shifts from the wave crest (resp. trough) towards the forward (resp. backward) slope, where $c-\langle u\rangle$ increases (resp. decreases) (figure 4*a,b*). This near-surface shifting of $\partial\langle u\rangle/\partial z$ causes fluid particles to experience positive (resp. negative) $\partial\langle u\rangle/\partial z$ for a shorter (resp. longer) time than in the deep region. As a result, $\overline{\partial\langle u\rangle/\partial z}^L$ decreases in the near-surface region.

5.2. *Wave Lagrangian effect on turbulence vorticity*

In this section, we analyse the cumulative effect of a surface wave on turbulence vorticity evolution using the Lagrangian average. The vorticity evolution equations in the Earth-fixed frame are given in appendix C. To avoid the artificial cancellation in the statistics due to the opposite signs of positive and negative turbulence vorticity, we modify the vorticity evolution equations by multiplying $\mathrm{sgn}(\omega_x)$ (resp. $\mathrm{sgn}(\omega_z)$) on the two sides of (C 1) (resp. (C 2)). Here, $\mathrm{sgn}(\cdot)=(\cdot)/|\cdot|$ is a signum function. In other words, we investigate the evolution of positive and negative vortices separately to remove the potential false indication of vortices cancellation in the overall statistics. We further apply the Lagrangian average operator (A 2) to the equations. Our results show that there are four dominant terms, namely

$$\underbrace{\overline{\mathrm{sgn}\,(\omega_x)\,\omega_z\frac{\partial\langle u\rangle}{\partial z}}^L}_{\mathscr{T}_{x,w}},\quad \underbrace{\overline{\mathrm{sgn}\,(\omega_x)\,\omega_x\frac{\partial u'}{\partial x}}^L}_{\mathscr{S}_{x,t}},\quad \underbrace{\overline{\mathrm{sgn}\,(\omega_z)\,\omega_x\frac{\partial\langle w\rangle}{\partial x}}^L}_{\mathscr{T}_{z,w}},\quad \underbrace{\overline{\mathrm{sgn}\,(\omega_z)\,\omega_z\frac{\partial w'}{\partial z}}^L}_{\mathscr{S}_{z,t}}. \tag{5.3}$$

Here, $\mathscr{T}_{x,w}$ and $\mathscr{T}_{z,w}$ represent the cumulative contributions to the streamwise and vertical vortices due to the tilting of vertical and streamwise vortices, respectively, by the wave motion; $\mathscr{S}_{x,t}$ and $\mathscr{S}_{z,t}$ represent the vortex stretching effect by turbulence velocity fluctuations. Note that the net stretching of streamwise and vertical vortices by the wave motion, $\overline{\mathrm{sgn}(\omega_x)\omega_x\partial\langle u\rangle/\partial x}^L$ and $\overline{\mathrm{sgn}(\omega_z)\omega_z\partial\langle w\rangle/\partial z}^L$, are omitted here because they are found to be small. Their small magnitude is caused by the symmetric distribution of ω_x and ω_z (figure 7*a,c*) together with the antisymmetric distribution

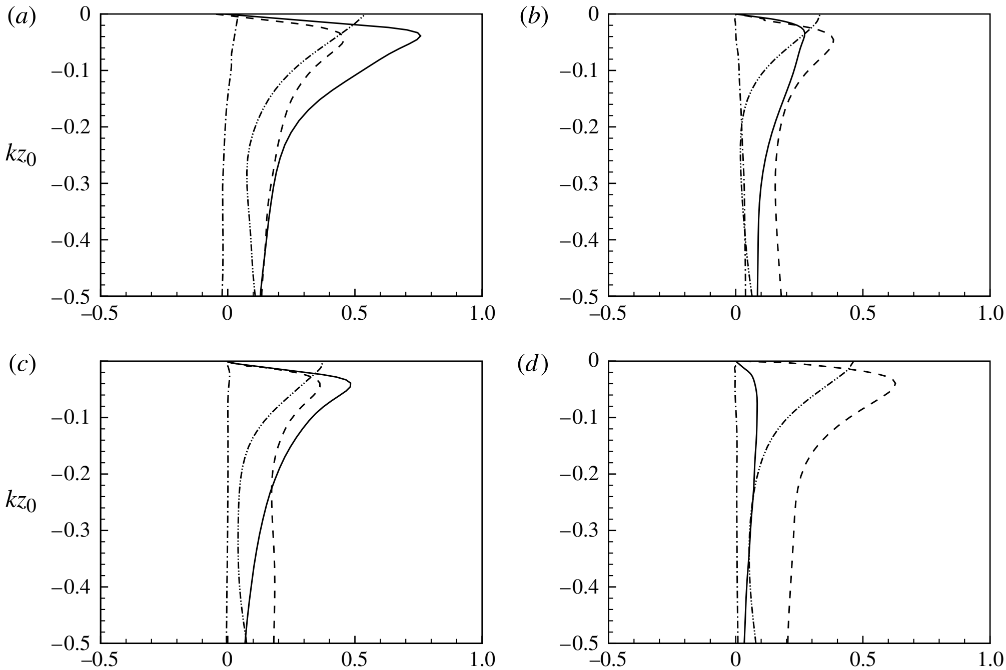

FIGURE 12. Vertical profiles of Lagrangian-averaged turbulence vorticity evolution terms: $\mathscr{T}_{x,w}$ (——), $\mathscr{S}_{x,t}$ (– – –), $\mathscr{T}_{z,w}$ (– · – · –), $\mathscr{S}_{z,t}$ (– ·· – ·· –) for (*a*) case I$_{15}$, (*b*) case II$_{10}$, (*c*) case II$_{15}$, and (*d*) case III$_{10}$. The results are normalized by $\omega_i^{rms,cf} u_i^{\prime rms,cf}/L_\infty^{cf}$.

of $\partial\langle u\rangle/\partial x$ and $\partial\langle w\rangle/\partial z$ (figure 4*c*) with respect to the wave crest (as well as the trough). As a result, the stretching of streamwise vortices (resp. the compression of vertical vortices) under the backward slope is nearly cancelled by the compression of streamwise vortices (resp. the stretching of vertical vortices) under the forward slope as far as the Lagrangian average is concerned.

Figure 12 shows the profiles of $\mathscr{T}_{x,w}$, $\mathscr{S}_{x,t}$, $\mathscr{T}_{z,w}$, and $\mathscr{S}_{z,t}$. We first focus on case II$_{10}$ shown in figure 12(*b*). We can see that as the free surface is approached, $\mathscr{T}_{x,w}$ is positive, increases to a maximum value, and then decreases sharply. The positive value indicates that vertical vortices are tilted in the wave propagation direction to contribute to the growth of streamwise vortices. The variation of $\mathscr{T}_{x,w}$ can be related to $\overline{\partial\langle u\rangle/\partial z}^L$ and is discussed later in this section.

Next, we discuss the vortex tilting term for vertical vortices, $\mathscr{T}_{z,w}$. As shown in figure 12(*b*), interestingly, $\mathscr{T}_{z,w}$ is about zero at all the depths. Therefore, under wave distortion, the net effect of vortex tilting is only from the vertical direction towards the streamwise direction, and the strengthened streamwise vortices are not tilted back to replenish the weakened vertical vortices. This phenomenon is consistent with the vorticity distribution result in § 4, which shows that vertical vortices tilt towards the wave propagation direction, whereas streamwise vortices oscillate around the horizontal without an overall net inclination angle. The small magnitude of $\mathscr{T}_{z,w}$ is somewhat surprising, because the positive $\overline{\partial\langle w\rangle/\partial x}^L$ (figure 10) may suggest a net anticlockwise turning of streamwise vorticity by the wave motion. Note that although $\mathscr{T}_{z,w}$ is usually ignored in previous studies of wave–turbulence interaction, the reason for doing this is not obvious. Later in this section, further analysis will be provided to answer this question.

Figure 12(*b*) also shows that both $\mathscr{S}_{x,t}$ and $\mathscr{S}_{z,t}$ are positive, indicating that the vortex stretching by turbulence velocity fluctuations is important for both the streamwise and vertical vortices in their Lagrangian evolution.

Next, we compare cases I_{15} (figure 12*a*), II_{15} (figure 12*c*), and III_{10} (figure 12*d*) with case II_{10} (figure 12*b*). The variations of $\mathscr{S}_{x,t}$, $\mathscr{T}_{z,w}$, and $\mathscr{S}_{z,t}$ are similar. Due to the different wave strain rate, the magnitude of $\mathscr{T}_{x,w}$ in cases I_{15} and III_{10} is larger and smaller than that in case II_{10}, respectively. The magnitude of $\mathscr{T}_{x,w}$ in case II_{15} is larger than that in case II_{10}, due to the stronger wave nonlinearity in case II_{15}. It is noted that the turbulence stretching is important for all the cases. The turbulence stretching even dominates the vortex tilting by the wave in case III_{10}, whereas it is about the same as or slightly smaller than the vortex tilting by the wave in the other cases. This result is consistent with the relatively large and small tilting of vertical vortices in cases I_{15}, II_{10}, and II_{15} and case III_{10}, respectively, shown in § 4.3.

To understand the contribution from the Lagrangian wave properties and the correlation between the wave and turbulence to the vortex tilting, we perform Reynolds decomposition for $\mathscr{T}_{x,w}$ and $\mathscr{T}_{z,w}$ based on Lagrangian averaging (see (A 4)), that is,

$$\overline{\mathrm{sgn}\,(\omega_x)\,\omega_z\frac{\partial\langle u\rangle}{\partial z}}^L = \underbrace{\overline{\mathrm{sgn}\,(\omega_x)\,\omega_z}^L\,\overline{\frac{\partial\langle u\rangle}{\partial z}}^L}_{\mathscr{T}_{x,w}^{LL}} + \underbrace{\overline{(\mathrm{sgn}\,(\omega_x)\,\omega_z)^l\frac{\partial\langle u\rangle}{\partial z}^l}^L}_{\mathscr{T}_{x,w}^{ll}}, \tag{5.4}$$

$$\overline{\mathrm{sgn}\,(\omega_z)\,\omega_x\frac{\partial\langle w\rangle}{\partial x}}^L = \underbrace{\overline{\mathrm{sgn}\,(\omega_z)\,\omega_x}^L\,\overline{\frac{\partial\langle w\rangle}{\partial x}}^L}_{\mathscr{T}_{z,w}^{LL}} + \underbrace{\overline{(\mathrm{sgn}\,(\omega_z)\,\omega_x)^l\frac{\partial\langle w\rangle}{\partial x}^l}^L}_{\mathscr{T}_{z,w}^{ll}}. \tag{5.5}$$

In (5.4) and (5.5), $\mathscr{T}_{x,w}^{LL}$ and $\mathscr{T}_{z,w}^{LL}$ denote the vortex tilting due to the Lagrangian-averaged strain field, and $\mathscr{T}_{x,w}^{ll}$ and $\mathscr{T}_{z,w}^{ll}$ denote the vortex tilting due to the correlation between the Lagrangian fluctuations of turbulence vorticity and wave strain rate.

Figure 13(*a*) shows the profiles of $\mathscr{T}_{x,w}^{LL}$ and $\mathscr{T}_{x,w}^{ll}$. As the wave surface is approached, $\mathscr{T}_{x,w}^{LL}$ increases to a maximum value and then decreases sharply. The variation of $\mathscr{T}_{x,w}^{LL}$ is related to $\overline{\partial\langle u\rangle/\partial z}^L$ (figure 10). The positive $\mathscr{T}_{x,w}^{LL}$ means that due to the Lagrangian accumulation of $\partial\langle u\rangle/\partial z$, vertical vortices are tilted clockwise. To the best of our knowledge, the result here is the first DNS evidence to support the theoretical description by Teixeira & Belcher (2002) (see their figure 8).

Besides $\mathscr{T}_{x,w}^{LL}$, the term $\mathscr{T}_{x,w}^{ll}$ also makes a positive contribution to the vortex tilting as shown in figure 13(*a*). Outside the Stokes layer, both ω_z (figure 7*c*) and $\partial\langle u\rangle/\partial z$ (figure 4*e*,*f*) reach maxima under the wave crest and minima under the wave trough. That is, there exists a positive correlation between ω_z and $\partial\langle u\rangle/\partial z$. Within the Stokes layer, due to the viscous effect of the free surface, $\partial\langle u\rangle/\partial z$ decorrelates with ω_z, leading to the reduction of $\mathscr{T}_{x,w}^{ll}$ towards the free surface. A comparison between the magnitude of $\mathscr{T}_{x,w}^{LL}$ and $\mathscr{T}_{x,w}^{ll}$ shows that near the wave surface, $\mathscr{T}_{x,w}^{LL}$ dominates $\mathscr{T}_{x,w}^{ll}$; in the deep region ($kz_0 < -0.3$), $\mathscr{T}_{x,w}^{LL}$ and $\mathscr{T}_{x,w}^{ll}$ are comparable.

Next, we discuss $\mathscr{T}_{z,w}^{LL}$ and $\mathscr{T}_{z,w}^{ll}$ shown in figure 13(*b*). As the wave surface is approached, $\mathscr{T}_{z,w}^{LL}$ increases to a maximum and then decreases. The increase of $\mathscr{T}_{z,w}^{LL}$

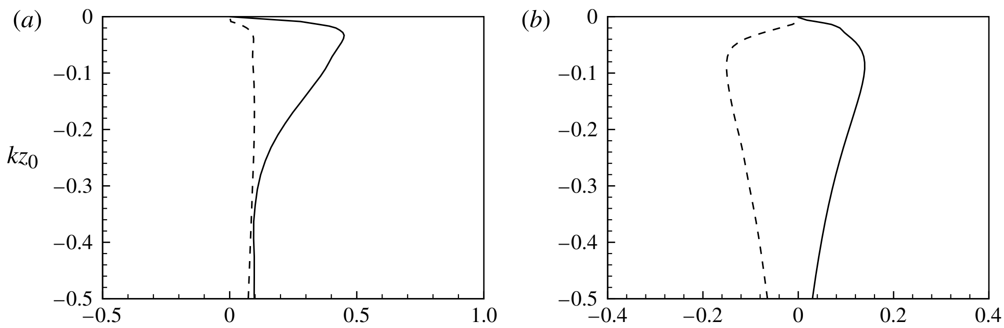

FIGURE 13. Vertical profiles of the contributions of the wave Lagrangian effect and wave–turbulence correlation to Lagrangian vortex tilting: (*a*) $\mathscr{T}^{LL}_{x,w}$ (——) and $\mathscr{T}^{ll}_{x,w}$ (– – –), and (*b*) $\mathscr{T}^{LL}_{z,w}$ (——) and $\mathscr{T}^{ll}_{z,w}$ (– – –). The results are normalized by $\omega_i^{rms,cf} u_i^{\prime rms,cf}/L_\infty^{cf}$. Case II_{10} is shown here.

is due to the increase of both $\overline{\partial\langle w\rangle/\partial x}^L$ and ω_x. As the wave surface is further approached, ω_x decreases due to the shear-free DBC (figure 7*a*). The $\mathscr{T}^{LL}_{z,w}$ is positive, indicating that the Lagrangian effect of the wave motion tilts streamwise vortices in the anticlockwise direction to contribute to the growth of vertical vortices. However, $\mathscr{T}^{ll}_{z,w}$ is negative due to the negative correlation between ω_x (figure 7*a*) and $\partial\langle w\rangle/\partial x$ (figure 4*d*). The $\mathscr{T}^{LL}_{z,w}$ and $\mathscr{T}^{ll}_{z,w}$ nearly cancel each other throughout all the depths (figure 13*b*). This cancellation can also be understood through the following scaling analysis. Using the definition of $\mathscr{T}^{LL}_{z,w}$ (5.5) and the fact that $\overline{\partial\langle w\rangle/\partial x}^L \sim O(akS)$ (figure 10), we estimate

$$\mathscr{T}^{LL}_{z,w} \sim O\left(\overline{\mathrm{sgn}\,(\omega_x)\,\omega_x}^L akS\right). \tag{5.6}$$

We estimate $\mathscr{T}^{ll}_{z,w}$ next. Due to the strong wave distortion effect, the evolution of ω_x is dominated by $\omega_x\partial\langle u\rangle/\partial x$ (see (C 1)), where $\partial\langle u\rangle/\partial x \sim O(ak\sigma)$. The horizontal variation of ω_x is small (see figure 7*a*). Therefore,

$$(\mathrm{sgn}\,(\omega_x)\,\omega_x)^l \sim \int \mathrm{sgn}\,(\omega_x)\,\omega_x \frac{\partial\langle u\rangle}{\partial x}\,\mathrm{d}t \approx \overline{\mathrm{sgn}\,(\omega_x)\,\omega_x}^L \int \frac{\partial\langle u\rangle}{\partial x}\,\mathrm{d}t \sim O\left(\overline{\mathrm{sgn}\,(\omega_x)\,\omega_x}^L ak\right). \tag{5.7}$$

A comparison between the distributions of ω_x and $\partial\langle w\rangle/\partial x$, shown respectively in figures 7(*a*) and 4(*d*), indicates that they are nearly negatively correlated. Using $(\partial\langle w\rangle/\partial x)^l \sim O(S)$ (figure 11), we estimate

$$\mathscr{T}^{ll}_{z,w} \sim O\left(-\overline{\mathrm{sgn}\,(\omega_x)\,\omega_x}^L akS\right), \tag{5.8}$$

which is the opposite of (5.6). The cancellation of $\mathscr{T}^{LL}_{z,w}$ and $\mathscr{T}^{ll}_{z,w}$ concludes the discussion earlier in this section that although the wave field exhibits non-zero $\overline{\partial\langle w\rangle/\partial x}^L$, there is still no net Lagrangian vortex tilting effect on streamwise vortices because of the offsetting effect by Lagrangian fluctuations.

As a summary, figure 9(*b*) illustrates the Lagrangian effect of waves on turbulence vorticity. Both the streamwise and vertical vortices are stretched by turbulence fluctuations. Vertical vortices are tilted in the streamwise direction by the mean Lagrangian wave effect as well as the correlation between the Lagrangian fluctuations of wave strain rate and turbulence vorticity. The net vortex tilting from the streamwise towards the vertical direction is negligible. Note that Craik (1977) and Leibovich (1977) explained the generation of Langmuir circulation using the Lagrangian effect of waves on the tilting of vertical vortices (the CL2 mechanism). In their analysis, vertical vortices are induced by a spanwise perturbation of a wind-driven streamwise current. Vertical vortices on the two sides of the perturbation have opposite signs of vertical vorticity and are tilted in the streamwise direction to develop Langmuir circulation. In our simulation, the turbulence vortices are generated in the bulk flow. In general, the turbulence vortices approach the surface individually, and vortex pairs are rare. As expected, Langmuir cells do not show in our result. (Note that there is no wind shear stress applied at the free surface in our simulation.) While Langmuir circulation is not the subject of the present study, a similar numerical investigation of the Lagrangian effect of waves on vorticity evolution can be performed in future study, in which wind-driven current will be included in the simulation as an extension of the present work. The detailed information on the wave and turbulence fields at different wave phases will then be valuable for a quantitative, mechanistic study of the CL2 process and Langmuir turbulence.

6. Conclusions

In this study, we have used DNS to investigate the effect of progressive surface waves on turbulence underneath. We focus on the fundamental physics, and accordingly set up the simulation with well-controlled isotropic turbulence generated in the bulk flow and an accurately produced wave with its amplitude precisely maintained. This set-up facilitates a mechanistic study with accurate quantification of wave properties and turbulence statistics. While this canonical problem does not include other complications such as wind stress, surface current, and wave breaking, it directly corresponds to the mechanistic studies in the literature with a similar setting, such as the theoretical analysis by Teixeira & Belcher (2002, 2010) and the laboratory experiments of mechanically generated waves passing through a grid-generated turbulence field (see e.g. Ölmez & Milgram 1992). This problem set-up has the advantage of being able to isolate fundamental processes of wave–turbulence interaction and use DNS as a research tool for the essential dynamics.

Because it is through the kinematic and dynamic boundary conditions at the wave's surface, the periodic distortion by the wave's orbital velocity, and the nonlinear wave effect that a surface wave affects the subsurface turbulence, we have examined the velocity and strain rate of the wave field to establish a physical basis for the study of wave–turbulence interaction. Under the wave's backward slope, fluid elements are stretched in the streamwise direction and compressed in the vertical direction by the wave's motion, and the process reverses under the forward slope. Under the wave's crest and trough, fluid elements are distorted by the irrotational 'shear' strain of the wave.

Our study of the frequency spectrum of turbulence velocity fluctuation shows that there exists strong interaction between the wave and turbulence. The interaction depends on wave nonlinearity and the time scale ratio between the wave and turbulence. Due to the periodic convection by surface wave motion, the turbulence is enhanced at harmonics of the dominant wave frequency. The spectrum exhibits a σ_t^{-3} decay rate beyond the dominant wave frequency, suggesting that the dynamics of turbulence is dominated by the forcing of the surface wave (Thais & Magnaudet 1996).

Our study of instantaneous turbulence vortices, statistics of enstrophy components, and histogram of the vortex inclination angle shows that turbulence vortices are mainly aligned in the streamwise and vertical directions, and their distributions are dependent on the wave phase. Due to the periodic stretching and compression by the wave, streamwise turbulence vorticity reaches its maximum magnitude under the wave trough and its minimum under the wave crest, while the opposite occurs for vertical vorticity. Under the wave crest, streamwise and vertical vortices are turned respectively in the anticlockwise and clockwise directions, and a reverse process happens under the wave trough. Overall, there exists net tilting of vertical vortices towards the wave propagation direction.

Besides the examination of wave and turbulence fields at various wave phases in the Eulerian frame, wave Lagrangian properties have also been quantified in this study for the investigation of the cumulative effect of waves on turbulence. The Lagrangian average of the wave strain rate is documented in detail, together with illustrations of the variation of strain rate along particle trajectories. Lagrangian analysis of vorticity evolution provides quantitative results of the net effect of the turning and stretching by wave straining and turbulence fluctuations over many wave periods. Overall, there exists a cumulative effect of the surface wave on tilting vertical vortices towards the wave propagation direction, whereas the net tilting of streamwise vortices is small. To understand this cumulative effect, we have performed Reynolds decomposition based on the Lagrangian average for vorticity evolution equations. It is found that both Stokes drift velocity and the correlation between wave strain rate and turbulence vorticity contribute to the net tilting of vertical vortices, whereas for streamwise vortices, these two factors offset each other and result in a negligible tilting effect.

This paper concentrates on the analysis of the mean flow and turbulence vorticity. In Part 2, further analysis of turbulence Reynolds shear and normal stresses and the energy transfer between the wave and turbulence is provided. It is noted that the present study focuses on the basic physics of wave–turbulence interaction. We consider, as an idealized canonical problem, isotropic turbulence generated in the bulk flow and progressive wave with a shear-free surface. This problem set-up is relevant to the ocean situation of a swell propagating through a previously wind-stirred turbulent upper ocean boundary layer when the wind dies down. In Part 2, quantification of swell decay rate due to wave–turbulence interaction is discussed. If we relax the Reynolds number constraint of DNS and scale other physical quantities according to a swell wavelength of $\Lambda = 100$ m, the wave amplitude is 2.39 m in cases I_{15} and II_{15} and is 1.59 m in cases II_{10} and III_{10}. The turbulence velocity fluctuation is 0.11 m s^{-1} in cases I_{15} and II_{10}, 0.17 m s^{-1} in case II_{15}, and 0.51 m s^{-1} in case III_{10}. This covers a range of typical ocean conditions with the turbulence level in case III_{10} being relatively higher than usual. Our results indicate that for the wave amplitude to decay by half (i.e. a 75 % reduction in wave energy), it takes about a day for cases I_{15}, II_{10}, and II_{15} and a few hours for case III_{10}. Our results are consistent with previous field measurement and model predictions. Our simulations also indicate that the decay rate increases with the increase of wave slope and turbulence intensity (for details see Part 2). For the scenario of three-way interactions among wind, surface waves, and turbulent ocean boundary layers, it is not directly addressed in the present simulation. In future follow-up work with the increase in computing power, a spectrum of surface waves and the effect of wind can be included in the computation. To set up the simulation, measurement will be valuable in providing information on the initial and boundary conditions. In future studies, many aspects of the wave–turbulence interaction processes discussed here, such as the tilting of vertical vortices, are relevant (e.g. to the initial development of small Langmuir cells: see Teixeira & Belcher 2002), and the simulation framework and the Eulerian and Lagrangian analysis tools developed in this study can be used when the research is extended to other flow regimes.

Acknowledgements

The support for this research by the Office of Naval Research (N00014-06-1-0073 and N00014-13-1-0370) is gratefully acknowledged. We also thank the referees for their comments and suggestions, which were very helpful for us to improve this paper from the previous version.

Appendix A. Average operator

For a quantity $f(x, y, z, t)$, we define a wave phase average operator as

$$\langle f \rangle (x, z) = \frac{1}{T_s} \frac{1}{L_y} \int_{L_y} \int_{T_s} f\,(x - ct, y, z, t)\; \mathrm{d}t\, \mathrm{d}y. \tag{A 1}$$

Here, T_s is the sampling duration; $c = \sigma/k$ is the wave phase speed; the wave phase is defined according to the first harmonic of the surface elevation given as $a\sin(kx - \sigma t)$. For the partition of wave and turbulence components, the mean field $\langle f \rangle$ corresponds to the wave part and the fluctuation $f' = f - \langle f \rangle$ corresponds to the turbulence part.

A Lagrangian average operator is defined by tracking a wave particle that is convected by the wave velocity (Andrews & McIntyre 1978), that is,

$$\bar{f}^L = \frac{1}{T_{s,L}} \int_{t_0}^{t_0 + T_{s,L}} f^{\boldsymbol{\varPi}}\,(\boldsymbol{x}_0, t)\; \mathrm{d}t. \tag{A 2}$$

Here, $T_{s,L}$ is the sampling duration; $f^{\boldsymbol{\varPi}}(\boldsymbol{x}_0, t) = f(\boldsymbol{x}_0 + \boldsymbol{\varPi}(\boldsymbol{x}_0, t), t)$, where $\boldsymbol{\varPi}(\boldsymbol{x}_0, t) = (\varPi_x, \varPi_z)$ is the displacement of the wave particle that is initially located at $(\boldsymbol{x}_0, t_0)$:

$$\varPi_x\,(\boldsymbol{x}_0, t) = \int_{t_0}^{t} \langle u \rangle \left(\boldsymbol{x}_0 + \boldsymbol{\varPi}, t'\right)\; \mathrm{d}t', \tag{A 3a}$$

$$\varPi_z\,(\boldsymbol{x}_0, t) = \int_{t_0}^{t} \langle w \rangle \left(\boldsymbol{x}_0 + \boldsymbol{\varPi}, t'\right)\; \mathrm{d}t'. \tag{A 3b}$$

For the study of the Lagrangian properties of surface waves in § 5.1, we take $T_{s,L} = T_L$, where T_L is the Lagrangian wave period defined as the time for a wave particle to reach the same position relative to the wave form (Longuet-Higgins 1986, figure 1). For the study of turbulence statistics in § 5.2, we take $T_{s,L} = 70T_L$ to ensure the convergence of statistics. The T_L is equal to approximately $1.04T$ in case I_{15}, $1.01T$ in case II_{10}, $1.03T$ in case II_{15}, and $1.01T$ in case III_{10}. The Lagrangian wave period T_L is slightly longer than the Eulerian wave period T, as previously derived in theoretical analysis (see e.g. Longuet-Higgins 1986) and observed in numerical simulation (see e.g. Chang, Chen & Liou 2009). Note that T is the time it takes for a fixed spatial position to experience the same wave phase again, whereas T_L is for a particle that is convected downstream with the Stokes drift and is thus longer than T. Lagrangian fluctuation is defined by

$$f^l = f - \bar{f}^L. \tag{A 4}$$

Because $\bar{f}^L$ is a function of the initial depth z_0, a natural choice for the starting point of the wave particle is at the place $kx_0 - \sigma t_0 = \pi$ or $kx_0 - \sigma t_0 = 0$, so that $\eta \approx a\sin(kx_0 - \sigma t_0) = 0$ and $z_0 \in [-\overline{H}, 0]$. Starting from other locations does not change the essential physics of the result, but the upper limit of z_0 is non-zero and it is thus less convenient.

The plane average is defined by

$$\bar{f}(z) \equiv \frac{1}{L_x L_y}\int_S f(\boldsymbol{x}, t)\, \mathrm{d}x\, \mathrm{d}y. \tag{A 5}$$

Appendix B. $\partial\langle u\rangle/\partial z$ at the wave surface

At the wave surface, $\partial\langle u\rangle/\partial z$ is related to $\partial\langle w\rangle/\partial x$ according to the shear-free DBC (2.5*a*), which is rewritten as

$$\frac{\left(1-\eta_x^2\right)\tau_{13} + 2\eta_x\tau_{33}}{1+\eta_x^2} = \frac{\left(1-\eta_x^2\right)\dfrac{1}{Re}\left(\dfrac{\partial\langle u\rangle}{\partial z} + \dfrac{\partial\langle w\rangle}{\partial x}\right) + 2\eta_x\dfrac{2}{Re}\dfrac{\partial\langle w\rangle}{\partial z}}{1+\eta_x^2} = 0. \tag{B 1}$$

Multiplying $Re(1+\eta_x^2)$ on both sides of (B 1) and regrouping the terms leads to

$$\frac{\partial\langle u\rangle}{\partial z} = -\frac{\partial\langle w\rangle}{\partial x} - \frac{4\eta_x}{1-\eta_x^2}\frac{\partial\langle w\rangle}{\partial z}. \tag{B 2}$$

The second term on the right-hand side of (B 2) is about one order of magnitude smaller than the first term (because $\eta_x \sim O(ak)$, while $\partial\langle w\rangle/\partial x$ and $\partial\langle w\rangle/\partial z$ are of the same order as S). Therefore, $\partial\langle u\rangle/\partial z$ and $\partial\langle w\rangle/\partial x$ at the wave surface are nearly negatively correlated (Longuet-Higgins 1992).

Appendix C. Vorticity evolution equations in the Earth-fixed frame

In the Earth-fixed frame, the evolution equations for ω_x and ω_z are

$$\frac{\mathrm{D}\omega_x}{\mathrm{D}t} = \underbrace{\omega_x\frac{\partial\langle u\rangle}{\partial x}}_{\mathrm{I}} + \underbrace{\omega_z\frac{\partial\langle u\rangle}{\partial z}}_{\mathrm{II}} + \underbrace{\omega_x\frac{\partial u'}{\partial x}}_{\mathrm{III}} + \underbrace{\omega_y\frac{\partial u'}{\partial y}}_{\mathrm{IV}} + \underbrace{\omega_z\frac{\partial u'}{\partial z}}_{\mathrm{V}} \underbrace{-\boldsymbol{u}'\boldsymbol{\cdot}\nabla\omega_x}_{\mathrm{VI}} + \underbrace{\frac{1}{Re}\nabla^2\omega_x}_{\mathrm{VII}}, \tag{C 1}$$

$$\frac{\mathrm{D}\omega_z}{\mathrm{D}t} = \underbrace{\omega_z\frac{\partial\langle w\rangle}{\partial z}}_{\mathrm{I}} + \underbrace{\omega_x\frac{\partial\langle w\rangle}{\partial x}}_{\mathrm{II}} + \underbrace{\omega_z\frac{\partial w'}{\partial z}}_{\mathrm{III}} + \underbrace{\omega_x\frac{\partial w'}{\partial x}}_{\mathrm{IV}} + \underbrace{\omega_y\frac{\partial w'}{\partial y}}_{\mathrm{V}} \underbrace{-\boldsymbol{u}'\boldsymbol{\cdot}\nabla\omega_z}_{\mathrm{VI}} + \underbrace{\frac{1}{Re}\nabla^2\omega_z}_{\mathrm{VII}}. \tag{C 2}$$

Here, $\mathrm{D}(\cdot)/\mathrm{D}t = \partial(\cdot)/\partial t + \langle\boldsymbol{u}\rangle\cdot\nabla(\cdot)$. Term I describes the vortex stretching due to the wave motion; term II describes the vortex turning by the wave; term III describes the stretching due to turbulence fluctuations; terms IV and V describe the turning due to turbulence fluctuations; term VI describes the transport of vorticity by turbulence velocity; and term VII describes the viscous diffusion of vorticity.

REFERENCES

ANDREWS, D. G. & MCINTYRE, M. E. 1978 An exact theory of nonlinear waves on a Lagrangian-mean flow. *J. Fluid Mech.* **89**, 609–646.

BORUE, V., ORSZAG, S. A. & STAROSELSKY, I. 1995 Interaction of surface waves with turbulence: direct numerical simulations of turbulent open-channel flow. *J. Fluid Mech.* **286**, 1–23.

BRUMLEY, B. H. & JIRKA, G. H. 1987 Near-surface turbulence in a grid-stirred tank. *J. Fluid Mech.* **183**, 235–263.

CAMPAGNE, G., CAZALBOU, J.-B., JOLY, L. & CHASSAING, P. 2009 The structure of a statistically steady turbulent boundary layer near a free-slip surface. *Phys. Fluids* **21**, 065111.

CAVALERI, L., ALVES, J.-H. G. M., ARDHUIN, F., BABANIN, A., BANNER, M., BELIBASSAKIS, K., BENOIT, M., DONELAN, M., GROENEWEG, J., HERBERS, T. H. C., HWANG, P., JANSSEN, P. A. E. M., JANSSEN, T., LAVRENOV, I. V., MAGNE, R., MONBALIU, J., ONORATO, M., POLNIKOV, V., RESIO, D., ROGERS, W. E., SHEREMET, A., MCKEE SMITH, J., TOLMAN, H. L., VAN VLEDDER, G., WOLF, J. & YOUNG, I. 2007 Wave modelling: the state of the art. *Prog. Oceanogr.* **75** (4), 603–674.

CHANG, H.-K., CHEN, Y.-Y & LIOU, J.-C. 2009 Particle trajectories of nonlinear gravity waves in deep water. *Ocean Engng* **36**, 324–329.

CHEN, J., MENEVEAU, C. & KATZ, J. 2006 Scale interactions of turbulence subjected to a straining–relaxation–destraining cycle. *J. Fluid Mech.* **562**, 123–150.

CRAIK, A. D. D. 1977 The generation of Langmuir circulations by an instability mechanism. *J. Fluid Mech.* **81**, 209–223.

CRAIK, A. D. D. & LEIBOVICH, S. 1976 A rational model for Langmuir circulations. *J. Fluid Mech.* **73**, 401–426.

DE ANGELIS, V., LOMBARDI, P. & BANERJEE, S. 1997 Direct numerical simulation of turbulent flow over a wavy wall. *Phys. Fluids* **9** (8), 2429–2442.

ELLIOTT, J. G. 1953 Interim report. *Tech. Rep.* contract NOy-12561, US Navy, Bureau Yards and Docks. Hydrodynamics Laboratory, California Institute of Technology.

FENTON, J. D. 1985 A fifth-order Stokes theory for steady waves. *J. Waterways Port Coast. Ocean Engng* **111** (2), 216–234.

FULGOSI, M., LAKEHAL, D., BANERJEE, S. & DE ANGELIS, V. 2003 Direct numerical simulation of turbulence in a sheared air–water flow with a deformable interface. *J. Fluid Mech.* **482**, 319–345.

GRANT, A. L. M. & BELCHER, S. E. 2009 Characteristics of Langmuir turbulence in the ocean mixed layer. *J. Phys. Oceanogr.* **39** (8), 1871–1887.

GUO, X. & SHEN, L. 2009 On the generation and maintenance of waves and turbulence in simulations of free-surface turbulence. *J. Comput. Phys.* **228**, 7313–7332.

GUO, X. & SHEN, L. 2010 Interaction of a deformable free surface with statistically steady homogeneous turbulence. *J. Fluid Mech.* **658**, 33–62.

GUO, X. & SHEN, L. 2013 Numerical study of the effect of surface wave on turbulence underneath. Part 2. Eulerian and Lagrangian properties of turbulence kinetic energy. *J. Fluid Mech.* (submitted).

HANDLER, R. A., SWEAN, T. F. Jr, LEIGHTON, R. I. & SWEARINGEN, J. D. 1993 Length scales and the energy balance for turbulence near a free surface. *AIAA J.* **31**, 1998–2007.

HODGES, B. R. & STREET, R. L. 1999 On simulation of turbulent nonlinear free-surface flows. *J. Comput. Phys.* **151**, 425–457.

HUNT, J. C. R. 1984 Turbulence structure in thermal convection and shear-free boundary layers. *J. Fluid Mech.* **138**, 161–184.

HUNT, J. C. R. & GRAHAM, J. M. R. 1978 Free-stream turbulence near plane boundaries. *J. Fluid Mech.* **84**, 209–235.

ISKANDARANI, M. & LIU, P. L.-F. 1991 Mass transport in two-dimensional water waves. *J. Fluid Mech.* **231**, 395–415.

JEONG, J. & HUSSAIN, F. 1995 On the identification of a vortex. *J. Fluid Mech.* **285**, 69–94.

JIANG, J.-Y. & STREET, R. L. 1991 Modulated flows beneath wind-ruffled, mechanically generated water waves. *J. Geophys. Res.* **96**, 2711–2721.

JIANG, J.-Y., STREET, R. L. & KLOTZ, S. P. 1990 A study of wave–turbulence interaction by use of a nonlinear water wave decomposition technique. *J. Geophys. Res.* **95**, 16037–16054.

KAWAMURA, T. 2000 Numerical investigation of turbulence near a sheared air–water interface. Part 2. Interaction of turbulent shear flow with surface waves. *J. Mar. Sci. Technol.* **5**, 161–175.

KIM, J. & MOIN, P. 1985 Application of a fractional-step method to incompressible Navier–Stokes equations. *J. Comput. Phys.* **59**, 308–323.

KITAIGORODSKII, S. A., DONELAN, M. A., LUMLEY, J. L. & TERRAY, E. A. 1983 Wave–turbulence interactions in the upper ocean. Part 2. Statistical characteristics of wave and turbulent components of the random velocity field in the marine surface layer. *J. Phys. Oceanogr.* **13**, 1988–1999.

KITAIGORODSKII, S. A. & LUMLEY, J. L. 1983 Wave–turbulence interactions in the upper ocean. Part 1. The energy balance of the interacting fields of surface wind waves and wind-induced three-dimensional turbulence. *J. Phys. Oceanogr.* **13**, 1977–1987.

KOMORI, S., KUROSE, R., IWANO, K., UKAI, T. & SUZUKI, N. 2010 Direct numerical simulation of wind-driven turbulence and scalar transfer at sheared gas–liquid interfaces. *J. Turbul.* **11**, 1–20.

KOMORI, S., NAGAOSA, N., MURAKAMI, Y., CHIBA, S., ISHII, K. & KUWAHARA, K. 1993 Direct numerical simulation of three-dimensional open-channel flow with zero-shear gas–liquid interface. *Phys. Fluids* A **5**, 115–125.

KUMAR, S., GUPTA, R. & BANERJEE, S. 1998 An experimental investigation of the characteristics of free-surface turbulence in channel flow. *Phys. Fluids* **10**, 437–456.

LEIBOVICH, S. 1977 Convective instability of stably stratified water in the ocean. *J. Fluid Mech.* **82**, 561–581.

LEIBOVICH, S. 1980 On wave–current interaction theories of Langmuir circulations. *J. Fluid Mech.* **99**, 715–724.

LI, M., GARRETT, C. & SKYLLINGSTAD, E. 2005 A regime diagram for classifying turbulent large eddies in the upper ocean. *Deep-Sea Res.* A **52**, 259–278.

LOMBARDI, P., DE ANGELIS, V. & BANERJEE, S. 1996 Direct numerical simulation of near-interface turbulence in coupled gas–liquid flow. *Phys. Fluids* **8** (6), 1643–1665.

LONGUET-HIGGINS, M. S. 1953 Mass transport in water waves. *Phil. Trans.* A **245**, 535–581.

LONGUET-HIGGINS, M. S. 1986 Eulerian and Lagrangian aspects of surface waves. *J. Fluid Mech.* **173**, 683–707.

LONGUET-HIGGINS, M. S. 1992 Capillary rollers and bores. *J. Fluid Mech.* **240**, 659–679.

LUMLEY, J. L. & TERRAY, E. A. 1983 Kinematics of turbulence converted by a random wave field. *J. Phys. Oceanogr* **13**, 2000–2007.

LUNDGREN, T. 2003 Linearly forced isotropic turbulence. *Tech. Rep.* 461. Center for Turbulence Research, Stanford, CA.

MAGNAUDET, J. & THAIS, L. 1995 Orbital rotational motion and turbulence below laboratory wind water waves. *J. Geophys. Res.* **100**, 757–771.

MCWILLIAMS, J. C., SULLIVAN, P. P. & MOENG, C.-H. 1997 Langmuir turbulence in the ocean. *J. Fluid Mech.* **334**, 1–30.

MOIN, P. & MAHESH, K. 1998 Direct numerical simulation: a tool in turbulence research. *Annu. Rev. Fluid. Mech.* **30** (1), 539–578.

MORINISHI, Y., LUND, T. S., VASILYEV, O. V. & MOIN, P. 1998 Fully conservative higher-order finite difference schemes for incompressible flow. *J. Comput. Phys.* **143** (1), 90–124.

MORISON, J. R. & CROOKE, R. C. 1953 The mechanics of deep water, shallow water, and breaking waves. *Tech. Rep.* 40. US Army, Corps of Engineers, Beach Erosion Board.

NAGAOSA, R. 1999 Direct numerical simulation of vortex structures and turbulent scalar transfer across a free surface in a fully developed turbulence. *Phys. Fluids* **11**, 1581–1595.

ÖLMEZ, H. S. & MILGRAM, J. H. 1992 An experimental study of attenuation of short water waves by turbulence. *J. Fluid Mech.* **239**, 133–156.

PAN, Y. & BANERJEE, S. 1995 A numerical study of free-surface turbulence in channel flow. *Phys. Fluids* **7**, 1649–1664.

PEROT, B. & MOIN, P. 1995 Shear-free turbulent boundary layers. Part 1. Physical insights into near-wall turbulence. *J. Fluid Mech.* **295**, 199–227.

PHILLIPS, O. M. 1961 A note on the turbulence generated by gravity waves. *J. Geophys. Res.* **66**, 2889–2893.

POPE, S. B. 2000 *Turbulent Flows*. Cambridge University Press.

RASHIDI, M., HETSRONI, G. & BANERJEE, S. 1992 Wave–turbulence interaction in free-surface channel flows. *Phys. Fluids* A **4**, 2727–2738.

ROSALES, C. & MENEVEAU, C. 2005 Linear forcing in numerical simulations of isotropic turbulence: physical space implementations and convergence properties. *Phys. Fluids* **17**, 095106.

SHEN, L., ZHANG, X., YUE, D. K. P. & TRIANTAFYLLOU, G. S. 1999 The surface layer for free-surface turbulent flows. *J. Fluid Mech.* **386**, 167–212.

TEIXEIRA, M. A. C. & BELCHER, S. E. 2000 Dissipation of shear-free turbulence near boundaries. *J. Fluid Mech.* **422**, 167–191.

TEIXEIRA, M. A. C. & BELCHER, S. E. 2002 On the distortion of turbulence by a progressive surface wave. *J. Fluid Mech.* **458**, 229–267.

TEIXEIRA, M. A. C. & BELCHER, S. E. 2010 On the structure of Langmuir turbulence. *Ocean Model.* **31**, 105–119.

TEJADA-MARTÍNEZ, A. E., GROSCH, C. E., GARGETT, A. E., POLTON, J. A., SMITH, J. A. & MACKINNON, J. A. 2009 A hybrid spectral/finite-difference large-eddy simulator of turbulent processes in the upper ocean. *Ocean Model.* **30**, 115–142.

TENNEKES, H. & LUMLEY, J. L. 1972 *A First Course in Turbulence*. MIT Press.

THAIS, L. & MAGNAUDET, J. 1996 Turbulent structure beneath surface gravity waves sheared by the wind. *J. Fluid Mech.* **328**, 313–344.

VARIANO, E. A. & COWEN, E. A. 2008 A random-jet-stirred turbulence tank. *J. Fluid Mech.* **604**, 1–32.

VERON, F., MELVILLE, W. K. & LENAIN, L. 2009 Measurements of ocean surface turbulence and wave–turbulence interactions. *J. Phys. Oceanogr.* **39**, 2310–2323.

WALKER, D. T., LEIGHTON, R. I. & GARZA-RIOS, L. O. 1996 Shear-free turbulence near a flat free surface. *J. Fluid Mech.* **320**, 19–51.

YANG, D. & SHEN, L. 2011 Simulation of viscous flows with undulatory boundaries. Part 1. Basic solver. *J. Comput. Phys.* **230**, 5488–5509.

YOSHIKAWA, I., KAWAMURA, H., OKUDA, K. & TOBA, Y. 1988 Turbulence structure in water under laboratory wind waves. *J. Phys. Soc. Japan* **44**, 143–156.

ZHOU, H. 1999 Numerical simulation of Langmuir circulations in a wavy domain and its comparison with the Craik–Leibovich theory. PhD thesis, Stanford University.